Elasticity of single-crystal periclase at high pressure and temperature: The effect of iron on the elasticity and seismic parameters of ferropericlase in the lower mantle

DAWEI FAN[1,2,3,*], SUYU FU[2], JING YANG[2,4], SERGEY N. TKACHEV[5], VITALI B. PRAKAPENKA[5], AND JUNG-FU LIN[2,*]

[1]Key Laboratory of High Temperature and High Pressure Study of the Earth's Interior, Institute of Geochemistry, Chinese Academy of Sciences, Guiyang, Guizhou 550081, China ORCID 0000-0001-7840-2075
[2]Department of Geological Sciences, Jackson School of Geosciences, The University of Texas at Austin, Austin, Texas 78712, U.S.A.
[3]Center for High Pressure Science and Technology Advanced Research (HPSTAR), Shanghai 130012, China
[4]Geophysical Laboratory, Carnegie Institution of Washington, Washington, D.C. 20015, U.S.A.
[5]Center for Advanced Radiation Sources, University of Chicago, Chicago, Illinois 60437, U.S.A.

ABSTRACT

In this study, we measured the sound velocities of single-crystal periclase by Brillouin light scattering (BLS) combined with in situ synchrotron X-ray diffraction (XRD) up to ~30 GPa and 900 K in an externally heated diamond-anvil cell (EHDAC). Our experimental results were used to evaluate the combined effects of pressure and temperature on the elastic moduli of single-crystal periclase using third-order Eulerian finite-strain equations. All of the elastic moduli increased with increasing pressure but decreased with increasing temperature, except the off-diagonal modulus C_{12}, which remained almost constant up to ~30 GPa and 900 K. The derived aggregate adiabatic bulk and shear moduli (K_{S0}, G_0) at ambient conditions were 162.8(±0.2) and 130.3(±0.2) GPa, respectively, consistent with literature results. The pressure derivatives of the bulk [$(\partial K_S/\partial P)_{300\,K}$] and shear moduli [$(\partial G/\partial P)_{300\,K}$] at ambient conditions were 3.94(±0.05) and 2.17(±0.02), respectively, whereas the temperature derivatives of these moduli [$(\partial K_S/\partial T)_P$ and $(\partial G/\partial T)_P$] at ambient conditions were –0.025(±0.001) and –0.020(±0.001) GPa/K, respectively. A comparison of our experimental results with the high-pressure (P) and high-temperature (T) elastic moduli of ferropericlase (Fp) in the literature showed that all the elastic moduli of Fp were linearly correlated with the FeO content up to approximately 20 mol%. These results allowed us to build a comprehensive thermoelastic model for Fp to evaluate the effect of Fe-Mg substitution on the elasticity and seismic parameters of Fp at the relevant P-T conditions of the lower mantle. Our modeling results showed that both the increase of the Fe content in Fp and the increasing depth could change the compressional wave anisotropy (AV_P) and shear wave splitting anisotropy (AV_S) of Fp in the upper parts of the lower mantle. Furthermore, using our modeling results here, we also evaluated the contribution of Fp to seismic lateral heterogeneities of thermal or chemical origin in the lower mantle. Both the thermally induced and Fe-induced heterogeneities ratios ($R_{S/P} = \partial \ln V_S/\partial \ln V_P$) of Fp from 670 to 1250 km along a representative lower mantle geotherm increased by ~2–5% and ~15%, respectively. The thermally induced $R_{S/P}$ value of Fp20 is ~30% higher than Fp10, indicating that the Fe content has a significant effect on the thermally induced $R_{S/P}$ of Fp. Compared to the seismic observation results ($R_{S/P} = 1.7$–2.0) in the upper regions of the lower mantle, the Fe-induced $R_{S/P}$ value of Fp is more compatible than the thermally induced $R_{S/P}$ value of Fp20 (the expected composition of Fp in the lower mantle) within their uncertainties. Thus, we propose that Fe-induced lateral heterogeneities can significantly contribute to the observed seismic lateral heterogeneities in the Earth's lower mantle (670–1250 km).

Keywords: Elasticity, periclase, Brillouin light scattering, lower mantle, diamond anvil cell

INTRODUCTION

Periclase (MgO) is a classic, simple oxide that crystallizes in the rock-salt structure with no known experimental phase transition up to 250 GPa at least (e.g., Dorfman et al. 2012; Duffy et al. 1995a; McWilliams et al. 2012). The rock-salt structured MgO also represents one of the most common yet simply structured materials in the deep Earth. The structure can potentially be stable up to approximately 400 GPa based on computational studies and laser shock experiments (e.g., Karki et al. 1997; Belonoshko et al. 2010; McWilliams et al. 2012; Coppari et al. 2013; Oganov et al.

2003). MgO also has very high melting temperatures compared to other mantle minerals (e.g., Zerr and Boehler 1994; Ito et al. 2004; McWilliams et al. 2012; Tateno et al. 2014; Kimura et al. 2017). The wide P-T stability of MgO covers relevant high P-T conditions of the deep earth (Duffy and Ahrens 1995) and possibly terrestrial planets or exoplanets (Coppari et al. 2013; Duffy et al. 2015; Bolis et al. 2016). Therefore, precise knowledge of the elastic properties of MgO under high P-T conditions is crucial for constructing a reliable mineralogical model of the Earth's lower mantle. There have been an increasing number of studies on the elastic behavior of MgO covering a range of high-pressure or high-temperature conditions using different techniques, including static XRD (e.g., Utsumi et al. 1998; Fei 1999; Dewaele et al. 2000; Speziale et

---

* E-mail: fandawei@vip.gyig.ac.cn and afu@jsg.utexas.edu

al. 2001; Jacobsen et al. 2008), BLS (e.g., Sinogeikin and Bass 2000; Zha et al. 2000; Murakami et al. 2009, 2012), ultrasonic interferometry (e.g., Yoneda 1990; Chen et al. 1998; Reichmann et al. 1998; Li et al. 2006), shockwave compressions (e.g., Duffy and Ahrens 1995; Coppari et al. 2013), as well as theoretical studies (e.g., Isaak et al. 1990; Karki et al. 1999; Matsui et al. 2000; Wu et al. 2008; Dorogokupets 2010). To date, however, the elasticity of single-crystal MgO at simultaneous high P-T conditions is limited to 8 GPa and 1600 K (Chen et al. 1998), much lower than the P-T conditions expected in the lower mantle, which extends at depths corresponding to pressures above 23 GPa.

MgO forms a solid solution with FeO, and in a MgO-rich composition, it is known as ferropericlase (Fp) (Mg,Fe)O while magnesiowustite is named for a FeO-rich composition. In the Earth's lower mantle, Fp is believed to be the second most abundant mineral, coexisting with the most abundant (Al,Fe)-bearing bridgmanite (Bgm) and Ca-perovskite (e.g., Ringwood 1975; Kung et al. 2002; Lin et al. 2005, 2006; Marquardt et al. 2009a, 2009b). Experiments on iron partitioning between Fp and Bgm [K_D = (Fe/Mg)^{Bgm}/(Fe/Mg)^{Fp}] at high P-T conditions suggest that the FeO content in Fp lies in the range of 10–20 mol% for potential compositional models of the lower mantle (e.g., Mao et al. 1997; Wood 2000; Andrault 2001; Irifune et al. 2010). The influences of Fe-Mg substitution on the physical properties of Fp, especially across its electronic spin transition, have recently attracted significant interest to further our understanding of seismic observations and the geodynamical processes of the lower mantle (e.g., Lin et al. 2006, 2013; Fei et al. 2007; Crowhurst et al. 2008; Marquardt et al. 2009; Wu and Wentzcovitch 2014; Muir and Brodholt 2015; Yang et al. 2015). The effect of Fe-Mg substitution on the elastic properties of Fp has been investigated for the whole MgO-FeO system (e.g., Jacobsen et al. 2002; Muir and Brodholt 2015). In particular, previous studies on the effect of FeO in Fp showed that the substitution of FeO strongly increased the density and reduced the velocities of Fp (e.g., Badro et al. 2003; Tsuchiya et al. 2006; Lin et al. 2013; Muir and Brodholt 2015; Yang et al. 2015). However, the fundamental question of how FeO substitution affects the elastic moduli of Fp at high P-T conditions still needs to be better addressed experimentally.

Recently, there have been several studies attempting to characterize the effects of FeO on the full elasticity of Fp at the high P or high P-T conditions of the lower mantle (e.g., Jacobsen et al. 2002; Jackson et al. 2006; Reichmann et al. 2008; Marquardt et al. 2009a; Yang et al. 2015, 2016). Single-crystal XRD and ultrasonic interferometry measurements of the full elastic moduli for a wide range of compositions in the MgO-FeO system at ambient conditions have been documented (Jacobsen et al. 2002). In situ ultrasonic interferometry together with synchrotron XRD measurements on polycrystalline MgO have also been conducted up to 23.6 GPa and 1650 K, and used to establish an independent absolute pressure scale at high P-T conditions (Li et al. 2006; Tange et al. 2009; Kono et al. 2010). However, ultrasonic technique measurements are limited in pressure (<30 GPa) and are most readily performed on polycrystalline samples (e.g., Kung et al. 2002; Li et al. 2005, 2006; Li and Zhang 2005), thus, they only provide limited information on the elastic properties of minerals. Nowadays, BLS coupled with diamond-anvil cells (DAC) is the most commonly used technique to measure the single-crystal elasticity of mantle

minerals (e.g., Duffy et al. 1995b; Sinogeikin and Bass 2002; Sang and Bass 2014; Yang et al. 2014; Wu et al. 2016; Fu et al. 2017). It has tremendous advantages at extremely high P-T conditions for optically transparent and translucent samples (e.g., Marquardt et al. 2009a; Yang et al. 2015) and to derive the complete elastic moduli of single-crystal materials (Speziale et al. 2014). BLS has been used to study the single-crystal elasticity of MgO at pressures up to 50 GPa at room temperature (Zha et al. 2000) and temperatures up to 2500 K at room pressure (Sinogeikin et al. 2000, 2004a). Simultaneous high P-T single-crystal elasticity studies of the candidate minerals (e.g., olivine, pyroxene, garnet, spinel, ringwoodite, and Fp) of the Earth's interior were also reported up to 50 GPa and 1300 K using the BLS technique (e.g., Mao et al. 2012, 2015; Lu et al. 2013; Yang et al. 2014, 2016; Zhang and Bass 2016; Duan et al. 2018). For the single-crystal elasticity of Fp, BLS coupled with an EHDAC was reported up to 50 GPa and 900 K (Yang et al. 2016), while the high-pressure single-crystal elasticity of Fp was reported up to 96 GPa at room temperature (Marquardt et al. 2009a; Yang et al. 2015). However, studying the single-crystal elasticity of Fp with more than 10 mol% FeO (hereafter written as Fp10) is difficult because Fp with a higher amount of FeO is known to be too optically dark to perform the BLS measurement. Using high-pressure inelastic X-ray scattering (IXS) measurements (Fiquet et al. 2004) of the acoustic phonon dispersions of Fp to derive the full elastic moduli could be a solution to these problems. However, the reported elastic moduli of Fp17 in high-pressure IXS measurements (Antonangeli et al. 2011) have been inconsistent with other experimental results (impulsive stimulated light scattering, and BLS) (e.g., Crowhurst et al. 2008; Marquardt et al. 2009a, 2009b) and theoretical predictions (e.g., Wentzcovitch et al. 2009; Wu et al. 2009). Thus, the reliability of the IXS experimental results has been questioned because the IXS technique is not a direct method to obtain velocities but uses the acoustic phonon dispersions at very high frequencies to extract the velocities (Fiquet et al. 2004), which rises to an inevitable bias in the velocities. Insofar, there is a lack of comprehensive knowledge on the elasticity of MgO and Fp at the relevant high P-T conditions of the lower mantle.

In this study, we simultaneously measured the acoustic wave velocities and density of single-crystal MgO at high P-T conditions up to ~30 GPa and 900 K using in situ BLS and XRD in an EHDAC. These results were then used to evaluate the high P-T effects on the sound velocities and elastic moduli of MgO. Using the obtained elastic moduli of MgO at high P-T conditions as an end-member reference, together with the elastic moduli of Fp from previous BLS studies, we built a comprehensive thermoelastic model of Fp with up to 20 mol% FeO at the high P-T conditions relevant to lower mantle. We also used these results to evaluate the effects of FeO substitution on the elasticity of Fp, including the acoustic wave velocity anisotropies and seismic parameters. Finally, we used our results to interpret the seismic anisotropy and heterogeneities of the Earth's lower mantle.

EXPERIMENTAL METHODS

A single-crystal MgO platelet of 10 ×10 mm square and 0.5 mm thick with (100) crystallographic orientation was purchased from MTI Corporation, which was grown by an arc melting method and natural cooling. The crystal platelet was >99.95% pure with no visible inclusions or microcracking. The X-ray rocking curve of the platelet showed an orientation of <100> ±0.2° on the crystal surface.

Analysis of the XRD patterns of the crystal showed a cubic rock-salt structure with a lattice parameter (a) of 4.2163(2) Å and a density (ρ) of 3.58(1) g/cm³ at ambient conditions.

To prepare our high P-T BLS and XRD experiments in an EHDAC, the platelet was polished down on both sides to approximately 20–30 μm thick in the (100) crystallographic orientation using 3M diamond lapping films with an average grain size of 0.3 μm. The thin polished platelet was then cleaved into several ~70 × 70 μm square pieces. Round Re disks of 250 μm thick and 3 mm in diameter were pre-indented to 50–60 μm thick using a pair of diamond anvils with 500 μm culets. Subsequently, a cylindrical 250 μm diameter hole was drilled in the pre-indented area and used as the sample chamber. An R-type thermocouple was used for the high-temperature measurements of the sample chamber in the EHDAC (Sinogeikin et al. 2006; Kantor et al. 2012; Yang et al. 2014, 2016; Mao et al. 2015). The thermocouple was attached to one of the diamond surfaces approximately 500 μm away from its culet and cladded with a ceramic adhesive (Resbond 920), which was thermally conductive and electrically insulating. The EHDAC was also equipped with an alumina ceramic holder that was coiled with two Pt wire strings; each was 200 μm diameter and 48 cm in length (Lu et al. 2013; Mao et al. 2015; Yang et al. 2016). The Pt wire heater had a resistance of approximately 1 Ω at ambient conditions. A single-crystal platelet was then placed into the sample chamber, together with gold (Au) powder as the pressure calibrant for the XRD experiments (Fei et al. 2007) as well as a few ruby spheres as pressure indicators for the neon gas-loading (Mao et al. 1986) (Fig. 1a). The neon pressure medium was loaded into the sample chamber using the gas loading system in the Mineral Physics Laboratory of the University of Texas in Austin (Lu et al. 2013; Mao et al. 2015; Yang et al. 2016).

We conducted the high P-T BLS combined with XRD measurements at beamline 13-BMD of the GeoSoilEnviroConsortium for the Advanced Radiation Sources (GSECARS) of the Advanced Photon Source (APS), Argonne National Laboratory (ANL). An incident X-ray beam of 0.3344 Å wavelength focused to 7 × 20 μm² diameter (Sinogeikin et al. 2006) was used to confirm the platelet orientation and to determine the unit-cell volume of the crystal in the EHDACs. To avoid oxidation and failure of the diamond anvils and Pt wires at high temperature, the EHDAC was mounted inside a water-cooled holder with 150 μm thick silica glass windows, and Ar with 2% H$_2$ gas mixture continuously flowed through the EHDAC during heating (Sinogeikin et al. 2006). To minimize pressure instability for each given heating run, the sample chamber was heated to a given temperature and then stabilized for at least 30 min, and its pressure was continuously monitored using XRD until the pressure was sufficiently stable for the BLS experiments. The pressure was determined from the measured lattice parameters of Au at high P-T using the third-order Birch-Murnaghan equation of state of Au (Fei et al. 2007), and

the temperature of the sample chamber was from the thermocouple measurements. BLS measurements were only conducted when no significant change in pressure was confirmed by the analysis of the XRD patterns of the Au calibrant. To ensure the pressure stability of the experiments a series of XRD patterns of the Au pressure calibrant were collected before and after the BLS measurements of pressure determinations at high P-T. The pressure uncertainties were determined using multiple measurements from the pressures before and after the BLS measurements for each P-T point. Temperatures of the sample chamber were actively stabilized within ±1 K using the temperature-power feedback program with a remotely controlled Tektronix Keithley DC power supply during the experiments (Sinogeikin et al. 2006). The uncertainties of the unit-cell parameters of MgO were typically in the order of 0.03% (Supplemental[1] Table S1), indicating that the MgO sample remained sufficiently high quality for the XRD and BLS experiments at high P-T conditions. Analysis of the XRD pattern of the sample was used to determine the density of MgO at each P-T condition before and after the BLS measurements.

The single-crystal XRD patterns (Fig. 1b) were also taken to verify the [100] crystallographic direction of the MgO platelet before carrying out the BLS measurements. Then, the motorized DAC rotation stage, which was perpendicular to the focused X-ray beam, was rotated by 45° to get the [110] crystallographic direction of the MgO platelet. Analysis of the XRD spots of the MgO crystal showed a high-quality single-crystal nature with a typical full-width at half maximum (FWHM) of a diffraction peak at ±0.2° (Fig. 1b). High P-T BLS spectra of the single-crystal MgO along the [100] and [110] crystallographic directions as well as XRD spectra were collected up to ~30 GPa at selected temperatures of 300, 500, 700, and 900 K (Figs. 2 and 3, and Supplemental[1] Table S1). The Brillouin system was equipped with a Coherent Verdi V2 solid-state laser with a wavelength of 532 nm, and a laser head power of 0.4 W was used for the BLS measurements. BLS spectra were collected in the symmetric forward scattering geometry with an external scattering angle of 50° using a six-pass Sandercock-type piezoelectrically scanning tandem Fabry-Pérot interferometer (Sandercock 1982). The interferometer was equipped with a Perkin Elmer MP983 photocounting module with a low dark count rate of <2 counts/s at room temperature (Sinogeikin et al. 2006). The laser beam focused on the sample position was approximately 15 μm in diameter. The external scattering angle of the system was calibrated using silicate glass and distilled water standards (Ostwald et al. 1977; Polian et al. 2002). The acoustic V_P and V_S velocities of the sample were derived from the analysis of the measured Brillouin frequency shift as follows:

$$V_{P,S} = (\lambda_0 \Delta v_B)/2\sin(\theta/2) \tag{1}$$

where $V_{P,S}$ is the acoustic compressional or shear wave velocity, respectively, λ_0 is the incident laser wavelength of 532 nm, Δv_B is the Brillouin frequency shift, and θ is the external scattering angle of 50°.
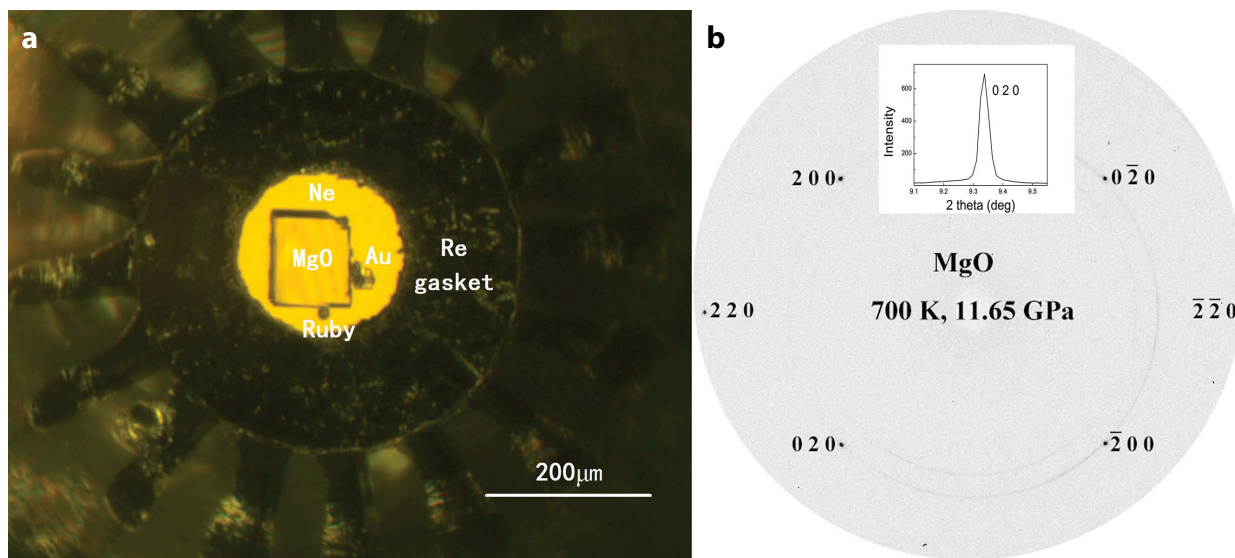

FIGURE 1. Representative sample chamber image and X-ray diffraction image along the principal crystallographic axis [100] of single-crystal MgO platelet at high P-T conditions. (**a**) MgO (100) platelet, together with Au and a ruby sphere calibrant, in Ne medium. (**b**) Representative X-ray diffraction pattern along the principal crystallographic axis [100] of single-crystal MgO platelet at 11.65 GPa and 700 K. The inset shows the high-quality single-crystal nature with a typical FWHM of a diffraction peak of MgO at ±0.2°. (Color online.)
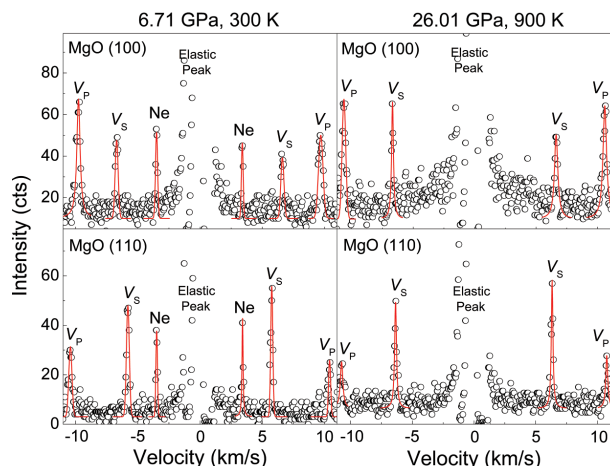
FIGURE 2. Representative Brillouin spectra of single-crystal periclase MgO at high pressure and temperature. Open circles = experimental data; solid lines = fitted V_P and V_S peaks, respectively. (Color online.)

RESULTS

Our collected BLS spectra along the [100] and [110] crystallographic directions showed strong V_P and V_S peaks with high signal-to-noise ratios at high P-T conditions (Fig. 2). Although two polarized V_S peaks were expected to exist, only one V_S peak was observed in our study. This is a result of the polarization of the V_S in the (100) crystallographic orientation of the MgO crystal interacting with the incident laser. Brillouin signals of the neon pressure medium were also observed at pressures below ~8 GPa, but they were too weak to be visible in the BLS spectra when the pressure was increased above approximately 8 GPa (Fig. 2). Analysis of the V_P and V_S velocities of MgO as a function of pressure at each given temperature showed that

the V_P along the [100] and [110] directions as well as V_S along the [110] direction (hereafter written as V_P[100], V_P[110], and V_S[110], accordingly) increased with increasing pressure and decreased with increasing temperature. However, V_S along the [100] (hereafter written as V_S[100]) remained almost unaffected by increasing P-T up to ~30 GPa and 900 K (Fig. 4). These observations indicate strong P-T effects on the V_S anisotropy.

The elastic tensors of cubic MgO can be fully described by three independent elastic moduli, C_{11}, C_{12}, and C_{44}. The use of the (100) platelets in this study permits determination of the elastic moduli (C_{11}, C_{12}, C_{44}) using the velocity determined in the [100] and [110] directions (Fig. 5), respectively, together with the measured density (Supplemental[1] Table S2). The equations used in the analysis were derived from Christoffel's equation (Grimsditch 2001):

$$\rho V_P^2[100] = C_{11} \tag{2}$$
$$\rho V_S^2[100] = C_{44} \tag{3}$$
$$\rho V_P^2[110] = (C_{11} + 2C_{44} + C_{12})/2 \tag{4}$$
$$\rho V_S^2[110] = (C_{11} - C_{12})/2 \tag{5}$$

where ρ is the density of MgO; V_P[100] and V_S[100] are the measured compressional- and shear-wave velocities of MgO along the [100] direction, respectively; V_P[110] and V_S[110] are the compressional- and shear-wave velocities along the [110] direction, respectively; and C_{11}, C_{12}, and C_{44} are the compressional, off-diagonal, and shear moduli of MgO, respectively. We used the least squares regression method utilizing the aforementioned four equations instead of only three equations for the modeling because examination of Equations 2–5 showed that the three elastic moduli (C_{11}, C_{12}, and C_{44}) could be determined more accurately. The uncertainties of the elastic moduli (Supplemental[1] Table S2) were estimated using standard error propagation in these derivations. We should note that these equations were derived from the general Christoffel's equation (Every 1980):
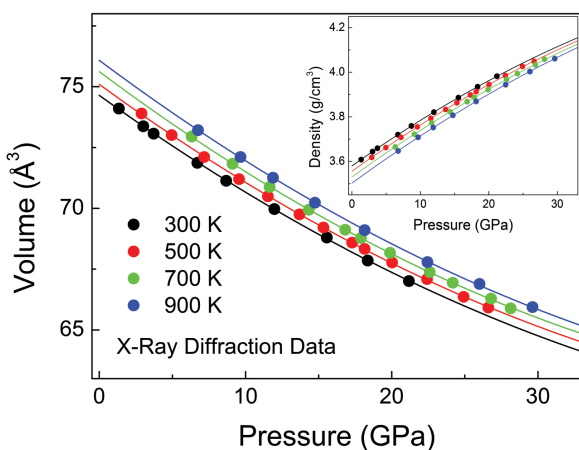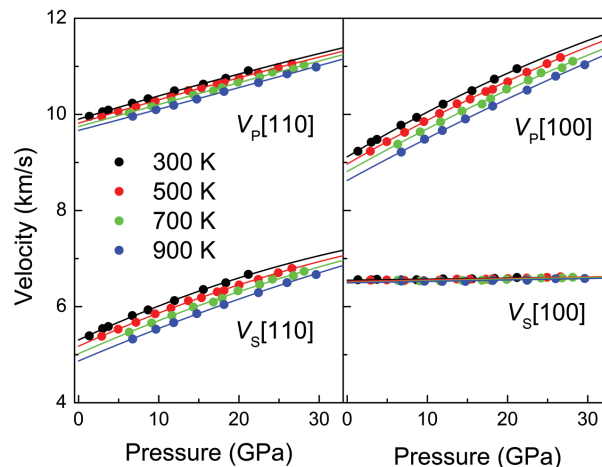

FIGURE 3. Pressure-volume-temperature relations of single-crystal periclase MgO. The results are derived from analysis of X-ray diffraction measurements in EHDACs. Solid symbols represent experimental data at 300, 500, 700, and 900 K. Solid lines are fits to experimental data using the third-order Birch-Murnaghan equation of state. The inset shows the density of MgO as a function of pressure at the given high temperatures. (Color online.)

FIGURE 4. Acoustic velocities of the single-crystal periclase MgO along the [110] and [100] crystallographic directions as a function of pressure and temperature. Solid circles = experimental data; solid lines = modeled results using the finite-strain theory. (Color online.)

$$\left| \Gamma_{ij} - \rho V^2 \delta_{ij} \right| = 0 \tag{6}$$

where ρ is the density from XRD measurements, V is the measured acoustic velocity, δ_{ij} is the Kronecker δ, and Γ_{ij} is the coefficient in the Christoffel matrix. The values of the Christoffel coefficients (Γ_{ij}) depend on the single-crystal constants (C_{ij}) in the reduced Voigt notation, where the propagation direction of the sound velocity is described by the direction cosines of the acoustic wavevector, n_i.

Using the derived elastic moduli of MgO, we calculated the aggregate adiabatic bulk and shear moduli (K_S and G) (Supplemental[1] Table S1 and Figs. 6a and 6b) using the Voigt-Ruess-Hill averages (Hill 1952):

$$K_S = C_{11} - 2C/3 \tag{7}$$
$$G = [(C/5 + 3C_{44}/5) + 5C_{44}C/(4C_{44} + 3C)]/2 \tag{8}$$
$$C = C_{11} - C_{12}. \tag{9}$$

The derived K_{S0} and G_0 at ambient conditions were 162.8($\pm$0.2) GPa and 130.3($\pm$0.2) GPa, respectively. The aggregate velocities of MgO (Figs. 6c and 6d) were calculated using the equations:

$$V_P = \sqrt{(K_S + 4G/3)/\rho} \tag{10}$$
$$V_S = \sqrt{G/\rho}. \tag{11}$$

The pressure and temperature derivatives of the elastic moduli were obtained by fitting the experimental data using the third-order finite strain equations (Tables 1 and 2) (Birch 1978; Duffy and Anderson 1989):

$$C_{ij}(T) = (1+2f)^{7/2}[C_{ij0}(T) + a_1 f] + a_2 P \tag{12}$$

$$C_{ij0}(T) = C_{ij0}(300\,K) + (T - 300)(\partial C_{ij}/\partial T)_P \tag{13}$$

$$a_1 = 3K_{T0}(T)[(\partial C_{ij}/\partial P)_T - a_2] - 7C_{ij0}(T) \tag{14}$$

$$f = (1/2)\{[V_0(T)/V]^{2/3} - 1\} \tag{15}$$

$$V_0(T) = V_0(300K)\exp\int_{300}^{T}\alpha dT \tag{16}$$

$$\left(\partial C_{ij}/\partial P\right)_T = \left(\partial C_{ij}/\partial P\right)_{300K}\exp\int_{300}^{T}\alpha dT. \tag{17}$$

where P is the measured pressure; $C_{ij0}(300\,K)$ is the elastic modulus at ambient conditions; $C_{ij0}(T)$ is the elastic modulus at temperature T and 1 bar; $C_{ij}(T)$ is elastic modulus at temperature T and high pressures; $(\partial C_{ij}/\partial T)_P$ is the temperature derivative of the elastic modulus at constant P and ambient T; $(\partial C_{ij}/\partial P)_T$ is the pressure derivative of the elastic modulus at constant T and ambient P; $(\partial C_{ij}/\partial P)_{300\,K}$ is the pressure derivative of the elastic modulus at ambient conditions; a_2 equals 3 for C_{11} and 1 for C_{12} and C_{44}; and f is the finite strain; V is the volume at high P-T determined by single-crystal XRD; $V_0(T)$ is the volume at 1 bar and high temperature; $V_0(300\,K)$ is the volume at ambient conditions; and α is the thermal expansion coefficient at ambient conditions. $K_{T0}(T)$ is the isothermal bulk modulus at temperature T and 1 bar, and can be calculated as:

$$K_{T0} = K_{T0}(300\,K) + (\partial K_T/\partial T)_P (T - 300) \tag{18}$$
$$K_{T0}(300) = K_{S0}(300\,K)/(1 + \alpha\gamma \times 300) \tag{19}$$
$$(\partial K_T/\partial T)_P \cong (\partial K_S/\partial T)_P/(1 + \alpha\gamma T) - K_S(T)/(1 + \alpha\gamma T)^2$$
$$[\alpha\gamma + \gamma T \times (\partial\alpha/\partial T)] \tag{20}$$

where α is the thermal expansion coefficient at ambient conditions, and γ is the Grüneisen parameter at ambient conditions with
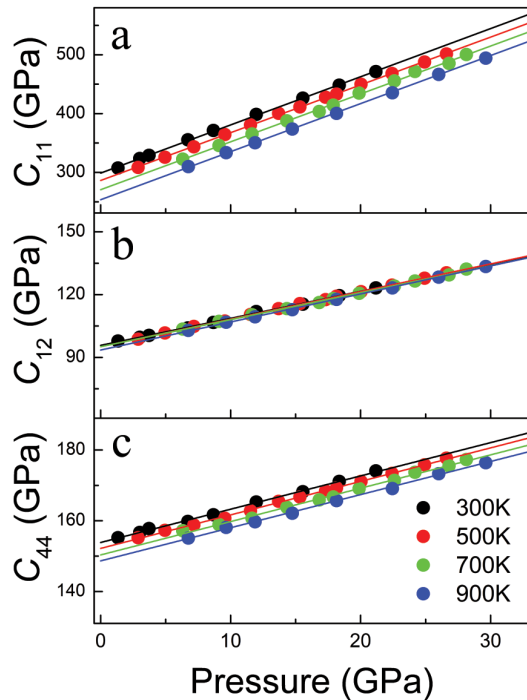

FIGURE 5. Single-crystal elastic moduli of periclase MgO as a function of pressure and temperature. Solid lines are the fitted results using the third-order finite-strain equation. (Color online.)
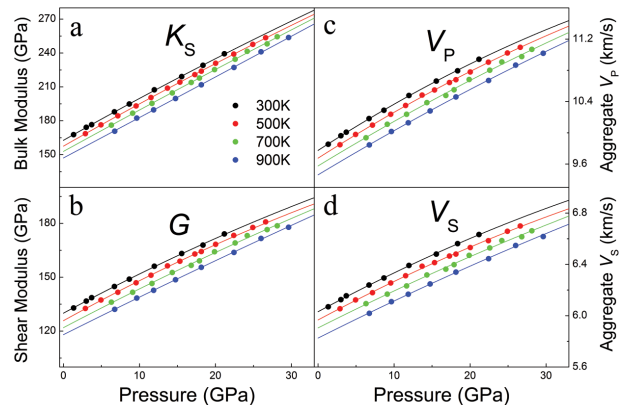

FIGURE 6. Aggregate elastic moduli and velocities of periclase MgO as a function of pressure and temperature. Solid lines are fits to the experimental data using the third-order finite-strain equation. (Color online.)

a literature value of 1.442 (Tange et al. 2009). The temperature derivative of K_S, $(\partial K_S/\partial T)_P$, and the pressure derivative of K_S, $(\partial K_S/\partial P)_T$, were derived by fitting K_S at high P-T using the third-order finite strain equations (Tables 1 and 2):

$$K_S = K_{S0}(1 + 2f)^{5/2}\{1 + [3(\partial K_S/\partial P)_T - 5]f\} \tag{21}$$

$$K_{S0} = K_{S0}(300\ \text{K}) + (\partial K_S/\partial T)_P(T - 300) \tag{22}$$

$$\left(\partial K_S / \partial P\right)_T = \left(\partial K_S / \partial P\right)_{300} \exp \int_{300}^{T} \alpha dT \tag{23}$$

where $K_{S0}(300\ \text{K})$ is the adiabatic bulk modulus at ambient conditions, $K_{S0}(T)$ is the adiabatic bulk modulus at temperature T and 1 bar, $K_S(T)$ is the adiabatic bulk modulus at temperature T and high pressures, and $(\partial K_S/\partial P)_{300\ \text{K}}$ is the pressure derivative of K_S at ambient conditions. We also constrained the pressure and temperature derivatives of the shear modulus G of MgO using the third-order finite strain equations:

$$G(T) = (1 + 2f)^{5/2}[G_0(T) + b_1 f] \tag{24}$$

$$G_0(T) = G_0(300\ \text{K}) + (\partial G/\partial T)_P(T - 300) \tag{25}$$

$$b_1 = 3K_{S0}(T)(\partial G/\partial P)_T - 5G_0(T) \tag{26}$$

$$\left(\partial G / \partial P\right)_T = \left(\partial G / \partial P\right)_{300\text{K}} \exp \int_{300}^{T} \alpha dT \tag{27}$$

where $G_0(300\ \text{K})$ is the shear modulus at ambient conditions; $G_0(T)$ is the shear modulus at temperature T and 1 bar; $G(T)$ is the shear modulus at temperature T and high pressures; $(\partial G/\partial P)_T$ and $(\partial G/\partial T)_P$ are the pressure and temperature derivatives of the shear modulus, respectively, and $(\partial G/\partial P)_{300\ \text{K}}$ is the pressure derivative of the shear modulus at ambient conditions (Tables 1–2).

DISCUSSION

The single-crystal elasticity of MgO at high P-T

By combining the BLS and single-crystal XRD measurements, we derived the full single-crystal elasticity of MgO at simultaneously high P-T conditions, including all of the elastic moduli (C_{ij} values, K_S, and G) (Figs. 5 and 6, Supplemental[1] Tables S1 and S2). All C_{ij} values and K_S exhibit a linear increase with pressure at the given temperatures (Figs. 5 and 6a), whereas G shows a slight pressure-dependent concave curvature (Fig. 6b). Compared with the values from ultrasonic interferometry and BLS experiments, the derived pressure derivatives for the compressional moduli C_{11}, off-diagonal moduli C_{12}, and bulk modulus K_S at ambient conditions in this study are slightly lower than the corresponding values in the literature (Jackson and Niesler 1982; Yoneda 1990; Sinogeikin and Bass 2000; Li et al. 2006; Kono et al. 2010), except the pressure derivative of C_{12} and K_S from previous BLS studies (Sinogeikin and Bass 2000; Zha et al. 2000), which are consistent with the results in this study. This indicates an enhanced temperature effect on these elastic moduli at high pressures. In addition, the pressure derivatives of the shear moduli (C_{44} and G) at ambient conditions are indistinguishable from the values in previous studies within experimental uncertainties (Tables 1 and 2), except a larger pressure derivative of G at ambient conditions was reported by Zha

TABLE 1. Single-crystal elastic moduli and their pressure and temperature derivatives of MgO at ambient conditions

Study	Methods[a]	C_{11} (GPa)	C_{12} (GPa)	C_{44} (GPa)	$(\partial C_{11}/\partial P)_{300\ \text{K}}$	$(\partial C_{12}/\partial P)_{300\ \text{K}}$	$(\partial C_{44}/\partial P)_{300\ \text{K}}$	$(\partial C_{11}/\partial T)_P$ (GPa/K)	$(\partial C_{12}/\partial T)_P$ (GPa/K)	$(\partial C_{44}/\partial T)_P$ (GPa/K)
This study	BLS	297.9(6)	95.1(5)	152.8(4)	8.35(5)	1.46(2)	1.26(3)	−0.062(3)	0.001(2)	−0.010(2)
Sinogeikin and Bass (2000)	BLS	298(2)	96(1)	154(2)	9.1(2)	1.3(2)	0.8(2)	_[b]	_[b]	_[b]
Sinogeikin et al. (2000)	BLS	_[b]	_[b]	_[b]	_[b]	_[b]	_[b]	−0.060(2)	0.001(1)	−0.015(1)
Zha et al. (2000)	BLS	297.0(1)	95.2(7)	155.7(5)	_[b]	_[b]	_[b]	_[b]	_[b]	_[b]
Jackson and Niesler (1982)	UI	296.8[c]	95.3[c]	155.8[c]	9.17[c]	1.61[c]	1.11[c]	_[b]	_[b]	_[b]
Yoneda (1990)	UI	297.8[c]	95.1[c]	155.8(2)	8.76[c]	1.81[c]	1.31[c]	_[b]	_[b]	_[b]
Sumino et al. (1983)	RPR	297(1)	96(1)	156.2(3)	_[b]	_[b]	_[b]	−0.0596[c]	0.0068[c]	−0.0122(2)
Isaak et al. (1989)	RPR	299.0(4)	96.4(6)	157.1(3)	_[b]	_[b]	_[b]	−0.0585[c]	0.0075[c]	−0.0126[c]
Karki et al. (1999)	DFT	300[c]	94[c]	147[c]	_[b]	_[b]	_[b]	−0.0598[c]	0.0089[c]	−0.0088[c]

[a] BLS = Brillouin light scattering; UI = ultrasonic interferometer; RPR = rectangular parallelepiped resonance; and DFT = density functional theory.
[b] The value is not available in the text.
[c] The uncertainty is not available in the text.

TABLE 2. Bulk and shear moduli and their pressure and temperature derivatives of MgO at ambient conditions

References	Methods[a]	K_{S0} (GPa)	G_0 (GPa)	$(\partial K_S/\partial P)_{300\ \text{K}}$	$(\partial G/\partial P)_{300\ \text{K}}$	$(\partial K_S/\partial T)_P$ (GPa/K)	$(\partial G/\partial T)_P$ (GPa/K)
This study	BLS	162.8(2)	130.3(2)	3.94(5)	2.17(2)	−0.025(1)	−0.020(1)
Sinogeikin and Bass (2000)	BLS	163(1)	130(1)	4.0(1)	2.4(1)	_[b]	_[b]
Sinogeikin et al. (2000)	BLS	_[b]	_[b]	_[b]	_[b]	−0.019(2)	−0.024(2)
Zha et al. (2000)	BLS	162.5(7)	130(2)	3.99(3)	2.85(9)	_[b]	_[b]
Murakami et al. (2009)	BLS	_[b]	130(3)	_[b]	1.9(1)	_[b]	_[b]
Murakami et al. (2012)	BLS	_[b]	_[b]	_[b]	_[b]	_[b]	−0.020(1)
Kono et al. (2010)	UI	162.0(4)	128.5(2)	4.27(3)	2.33(1)	−0.0184(4)	−0.0226(2)
Li et al. (2006)	UI	164(1)	129.8(6)	4.2(1)	2.42(6)	_[b]	_[b]
Yoneda (1990)	UI	162.7(2)	131.1[c]	4.1(3)	2.41[c]	_[b]	_[b]
Jackson and Niesler (1982)	UI	162.5(2)	130.9[c]	4.13(9)	2.53[c]	_[b]	_[b]
Sumino et al. (1983)	RPR	163(1)	133.9(2)	_[b]	_[b]	−0.018(2)	−0.021(1)
Isaak et al. (1989)	RPR	163.9(6)	131.8(5)	_[b]	_[b]	−0.0145[c]	−0.024[c]
Karki et al. (1997)	PP	159.7[c]	121.5[c]	4.26[c]	2.18[c]	_[b]	_[b]
Karki et al. (1999)	DFT	162[c]	128[c]	4.15[c]	2.44[c]	−0.014[c]	−0.0216[c]
Matsui et al. (2000)	MD	161[c]	131[c]	4.1[c]	2.4[c]	−0.028[c]	−0.024[c]

[a] PP = pseudopotential; and MD = Molecular Dynamic.
[b] The value is not available in the text.
[c] The uncertainty is not available in the text.

et al. (2000) and a smaller pressure derivative of C_{44} was reported by Sinogeikin and Bass (2000). These discrepancies are potentially due to the limited experimental pressure range or the possible distortion or deformation of MgO under high-pressure condition. At high temperature, all the elastic moduli follow similar trends with pressures (Figs. 5 and 6): increasing temperature offsets of C_{ij} values to a lower value at a given pressure, with the exception of those for the off-diagonal modulus C_{12}, which remain almost constant up to ~30 GPa and 900 K (Fig. 5). The temperature derivatives of the elastic moduli derived from our simultaneously high P-T measurements are consistent with literature experimental and theoretical results within their uncertainties (Tables 1 and 2). In particular, our $(\partial G/\partial T)_P$ is –0.020(1) GPa/K, which is in excellent agreement with another result [–0.020(1) GPa/K] from high P-T BLS measurements on polycrystalline MgO at T = 2700 K and P up to 68.4 GPa (Murakami et al. 2012). However, our $(\partial K_S/\partial T)_P$ is –0.025(1) (GPa/K), whose absolute value is slightly larger than those of most literature values (Isaak et al. 1989; Karki et al. 1999; Kono et al. 2010; Sinogeikin et al. 2000; Sumino et al. 1983), except the computational value of –0.028 (GPa/K) by Matsui et al. (2000). It is also worth noting that the temperature derivative of our C_{12} is very consistent with an earlier reported value obtained at 1 bar and high temperature (Sinogeikin et al. 2000), but it is substantially lower than previous rectangular parallelepiped resonance (RPR) experimental results (Isaak et al. 1989; Sumino et al. 1983) and a computational result (Karki et al. 1999). These discrepancies may be caused by the potential systematic errors in different experimental or theoretical methods.

Compressional wave velocity and shear wave splitting anisotropy of MgO

The elastic wave anisotropy of minerals expresses the difference in stiffness of a structure in different crystallographic directions, and shear wave anisotropy can be an indicator of the stability of minerals (Sinogeikin and Bass 2000). Knowledge of the velocity anisotropy of minerals at high P-T conditions may help to explain the seismic anisotropy within the Earth's interior (Long and Becker 2010; Mainprice 2015). To understand the evolution of the velocity anisotropy of MgO at high P-T conditions, the V_P and V_S velocities at different propagation directions and anisotropy distributions were calculated using our derived C_{ij} values and density at each given P-T point (Mainprice 1990; Mainprice et al. 2000). The percentage anisotropy for V_P (AV_P) is defined here as:

$$AV_P = (V_{P,max} - V_{P,min})/(V_{P,max} + V_{P,min}) \times 200\% \qquad (28)$$

where $V_{P,max}$ and $V_{P,min}$ represent the maximum and minimum V_P velocities, respectively. The polarization anisotropy factor of V_S (AV_S), also called the shear wave splitting factor, is the anisotropy percentage of the two V_S in a given direction and is defined as:

$$AV_S = (V_{S1} - V_{S2})/V_S \times 100\% \qquad (29)$$

where V_{S1} and V_{S2} are the two orthogonally polarized V_S velocities in the given propagation direction, and V_S represents the aggregate shear wave velocity. A contoured upper hemisphere stereogram of V_P and AV_S for MgO at two representative P-T conditions from our experiments is shown in Figure 7. These results show that, even though MgO is highly anisotropic at ambient conditions, with

an AV_P of 11.0% and AV_S of 21.5% (Fan et al. 2015; Mainprice 2015), AV_P reduces to 7.1% and AV_S to 14.1% at 7.17 GPa and 500 K in this study (Fig. 7). AV_P and AV_S decrease to 0.5 and 1.2%, respectively, at the maximum P-T conditions of 29.63 GPa and 900 K in our experiments, showing that MgO is almost elastically isotropic at such high P-T conditions (Fig. 7). These results clearly show that high P-T have a significant impact on the elastic wave velocity anisotropy of MgO.

Modeling the elasticity of (Mg,Fe)O ferropericlase at high P-T conditions

MgO is an end-member of (Mg,Fe)O ferropericlase, the second most abundant mineral in the lower mantle. Since the (Mg,Fe)O solid solution system crystallizes in the rock-salt structure at relevant lower-mantle P-T conditions, it is possible to use our MgO results as an end-member reference for understanding the elasticity of the (Mg,Fe)O system at high P-T conditions. To model the elasticity of Fp with different FeO contents at high P-T conditions, we initially compared our MgO results to literature elasticity values of Fp (Fp1, Fp6, and Fp10) derived from Brillouin measurements (Reichmann et al. 2008; Marquardt et al. 2009a; Yang et al. 2016) (Figs. 8 and 9). Considering the limited available single-crystal elastic moduli results of Fp from other methods (Jacobsen et al. 2002; Crowhurst et al. 2008; Antonangeli et al. 2011), and avoiding the potential systematic errors in different experimental methods (for example, incompatible results by IXS methods with other available studies; the possible effect on the pressure derivatives of elastic moduli by ultrasonic methods vs. Brillouin scattering), we only used literature Brillouin results in our modeling. We also limited the modeling to Fp with up to 20 mol% FeO because of the limited Fp compositions in the literature (Reichmann et al. 2008; Marquardt et al. 2009a; Yang et al. 2016) and the relevant Fp composition of approximately Fp20 in the Earth's lower mantle (Ringwood 1975; Mao et al. 1997; Wood 2000; Andrault 2001; Irifune et al. 2010).

Our analysis of the single-crystal elastic moduli (C_{ij}) of MgO as a function of the FeO content in mol% at ambient conditions showed that the substitution of FeO in Fp had a positive effect on C_{12} and a negative effect on C_{11} and C_{44}. Within experimental uncertainties, C_{12} linearly increased with FeO content, while C_{11} and C_{44} decreased linearly with increasing FeO content (Fig. 8):

$$C_{11} = 296.8(\pm 1.8) - 184.5(\pm 30.4)X_{Fe} \qquad (30)$$

$$C_{12} = 95.6(\pm 0.7) + 71.3(\pm 12.6)X_{Fe} \qquad (31)$$

$$C_{44} = 152.7(\pm 0.2) - 108.4(\pm 2.9)X_{Fe} \qquad (32)$$

where $X_{Fe} = M_{FeO}/(M_{FeO}+M_{MgO})$, X_{Fe} is the mole fraction, and M_{MgO} and M_{FeO} are the molar content. In addition, Jacobsen et al. (2002) reported the effects of FeO substitution on the C_{ij} values of (Mg,Fe)O using ultrasonic interferometry with high-frequency shear waves at ambient conditions. They fitted their C_{ij} values of the MgO-FeO system using a second-order or a third-order polynomial. A close inspection of the polynomial fits showed that there was a close linear relationship between the C_{ij} and FeO content when the FeO content in Fp is less than 20 mol% (as shown by the dashed lines in Fig. 8). Thus, we used the linear relationship between the C_{ij} and FeO content of Fp at ambient

conditions as a fitting parameter in our modeling here.

We also evaluated the high P-T relationship between the C_{ij} and FeO content by comparing the pressure and temperature derivatives of the single-crystal elastic moduli (C_{ij}) of MgO [$(\partial C_{ij}/\partial P)_{300 K}$ and $(\partial C_{ij}/\partial T)_P$] to the literature results of Fp (Fp6 and Fp10) (Marquardt et al. 2009a; Yang et al. 2016). Analysis of these results showed that within experimental uncertainties, $(\partial C_{11}/\partial P)_{300 K}$ and $(\partial C_{12}/\partial P)_{300 K}$ increased linearly with increasing FeO content, but $(\partial C_{44}/\partial P)_{300 K}$ decreased linearly with increasing FeO content (Fig. 9a):

$$(\partial C_{11}/\partial P)_{300 K} = 8.43(\pm0.13) + 2.68(\pm1.89)X_{Fe} \quad (33)$$

$$(\partial C_{12}/\partial P)_{300 K} = 1.46(\pm0.09) + 2.00(\pm1.22)X_{Fe} \quad (34)$$

$$(\partial C_{44}/\partial P)_{300 K} = 1.25(\pm0.01) - 4.31(\pm0.09)X_{Fe}. \quad (35)$$

Since the experimental temperature derivatives of C_{ij} [$(\partial C_{ij}/\partial T)_P$] of Fp were only available for Fp6 (Yang et al. 2016), we calculated the $(\partial C_{ij}/\partial T)_P$ of Fp10 using the C_{ij} values at ambient conditions obtained by Marquardt et al. (2009a) and C_{ij} values at high temperatures up to 4000 K obtained by Muir and Brodholt

(2015). The results above were then used to estimate the effect of FeO on the $(\partial C_{ij}/\partial T)_P$ of Fp. Within uncertainties, these results showed that $(\partial C_{11}/\partial T)_P$ and $(\partial C_{12}/\partial T)_P$ increased with increasing FeO content, while $(\partial C_{44}/\partial T)_P$ decreased with increasing FeO content. Therefore, we fitted the data with a linear relationship between the $(\partial C_{ij}/\partial T)_P$ and FeO content in Fp (Fig. 9b):

$$(\partial C_{11}/\partial T)_P = -0.063(\pm0.003) + 0.11(\pm0.03)X_{Fe} \quad (36)$$

$$(\partial C_{12}/\partial T)_P = 0.0010(\pm0.0006) + 0.08(\pm0.01)X_{Fe} \quad (37)$$

$$(\partial C_{44}/\partial T)_P = -0.01(\pm0.001) - 0.10(\pm0.02)X_{Fe}. \quad (38)$$

These derived linear relationships for the elastic moduli and their P-T derivatives were then combined with finite-strain theory equations (Eqs. 7–23) to evaluate the full elasticity of Fp at high P-T conditions. We should emphasize that these linear equations can only be used within the solid solution range of approximately 0–20 mol% FeO. Evaluation of the relationship between the elastic moduli and a higher FeO content at high P-T conditions in the (Mg,Fe)O system will require further experimental data in the future.
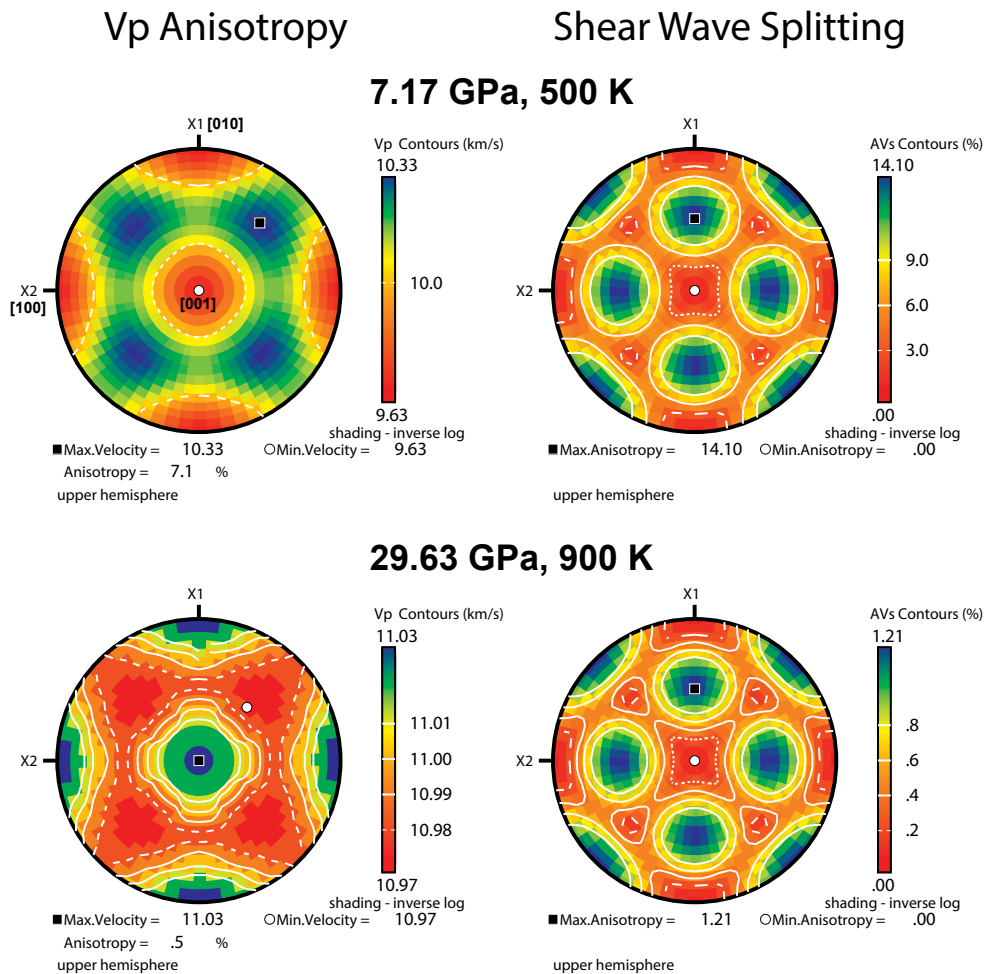

FIGURE 7. Upper hemisphere pole figures of V_P anisotropy and V_S splitting anisotropy of single-crystal periclase MgO at representative pressures and temperatures. Calculations were performed using the petrophysical software UnicefCareware of Mainprice (1990) with the derived single-crystal elastic moduli from this study. (Color online.)
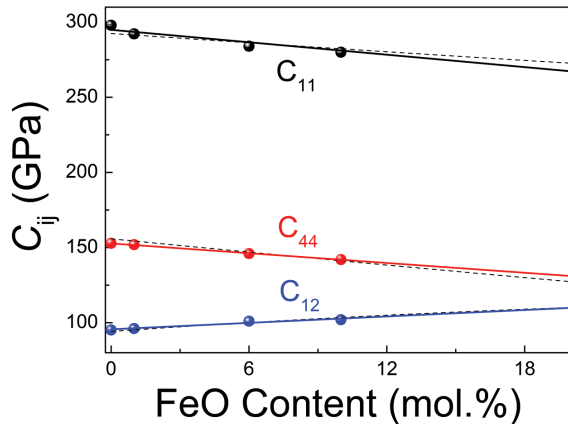
FIGURE 8. Single-crystal elastic moduli of ferropericlase (Mg,Fe)O as a function of the FeO content at ambient conditions. Solid symbols are experimental Brillouin light scattering results for MgO (this study), Fp1 (Reichmann et al. 2008), Fp6 (Yang et al. 2016), and Fp10 (Marquardt et al. 2009). Solid lines are linear fits to the Brillouin experimental data. Black dashed lines: ultrasonic results at ambient conditions by Jacobsen et al. (2002) for comparison. (Color online.)
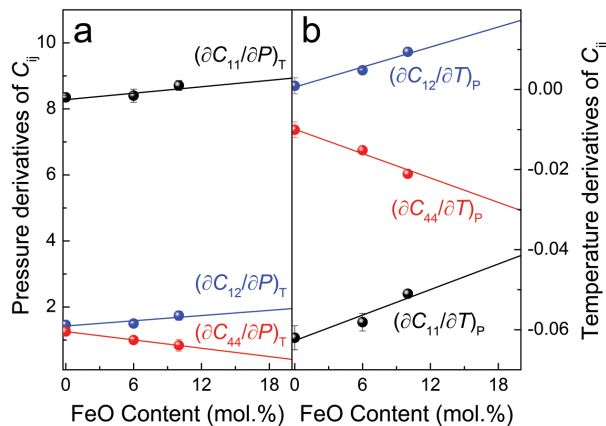

FIGURE 9. Pressure and temperature derivatives of the single-crystal elastic moduli of ferropericlase (Mg,Fe)O as a function of the FeO content at high P-T conditions. Solid symbols are derived from experimental Brillouin results for MgO (this study), Fp6 (Yang et al. 2016), and Fp10 (Marquardt et al. 2009). Solid lines are linear fits to the Brillouin experimental data. (Color online.)

FeO effects on the velocity profiles of Fp in the Earth's lower mantle

The Earth's mantle is generally believed to have a pyrolitic composition (Ringwood 1975). Based on the pyrolite model, Earth's lower mantle consists of approximately 75 vol% Bgm, 20 vol% Fp, and 5 vol% Ca-silicate perovskite (Ca-Pv) (Ringwood 1975; Irifune 1994; Ricolleau et al. 2009; Irifune et al. 2010). Although the exact composition of Earth's lower mantle has yet to be unambiguously determined, the current consensus is that Fp contains approximately 20 mol% FeO, while Bgm contains 10 mol% FeO, together with a few percents of Al_2O_3 in Bgm (e.g., Mattern et al. 2005; Lin and Tsuchiya 2008; Irifune et al. 2010; Lin et al. 2013). The spin transition in both Fp and (Al,Fe)-bearing

Bgm can also affect the iron partitioning between these phases (e.g., Irifune et al. 2010; Xu et al. 2017).

To better understand the influence of FeO on the velocity behavior of Fp, we calculated its velocity profiles using the Voigt-Reuss-Hill averages based on our high P-T elasticity modeling results for MgO and Fp (Fp10 and Fp20) along an expected mantle geotherm (Katsura et al. 2010) (Fig. 10). These modeled results were then compared with the velocity profiles of Bgm10 (with FeO content of 10 mol%) (Murakami et al. 2007; Chantel et al. 2012), Ca-Pv (Kudo et al. 2012), and the Preliminary Reference Earth Model (PREM) (Dziewonski and Anderson 1981) (Fig. 10). Briefly, the third-order Eulerian finite-strain equations and the third-order Birch-Murnaghan equation of state (Birch 1978) were used to evaluate the K_S and G of the relevant minerals by extrapolating the experimentally derived elastic moduli and their P-T derivatives to relevant P-T conditions. The reference P-T conditions at 670 km deep were ~23.8 GPa and ~1980 K, and the modeling depth was limited to 1250 km (mid-lower mantle) to avoid the complication of the potential effects of the iron electronic spin transition (e.g., see Lin et al. 2013 for a review).

Our modeled velocity profiles showed that substitution of FeO in Fp could significantly reduce both the V_P and V_S velocities at lower mantle conditions; compared to MgO, the V_P and V_S velocities of Fp20 were reduced by ~8% and ~10%, respectively. That is, $(\partial V_P/\partial X_{Fe})$ and $(\partial V_S/\partial X_{Fe})$ are approximately –0.04 and –0.03 km/s/X_{Fe}, respectively, in the upper part of the lower mantle. Furthermore, the V_P and V_S velocity profiles of Fp20 are ~8% and ~4% lower than the velocity profiles of the PREM, respectively. On the other hand, Bgm10 has the highest V_P profile and MgO has the highest V_S profile among all lower-mantle minerals, while Fp20 has the lowest V_P profile and Ca-Pv has the lowest V_S profile. The depth-dependent velocity profiles of a volume-weighted pyrolitic aggregate for the Earth's lower mantle, which was obtained from the arithmetic mean aggre-
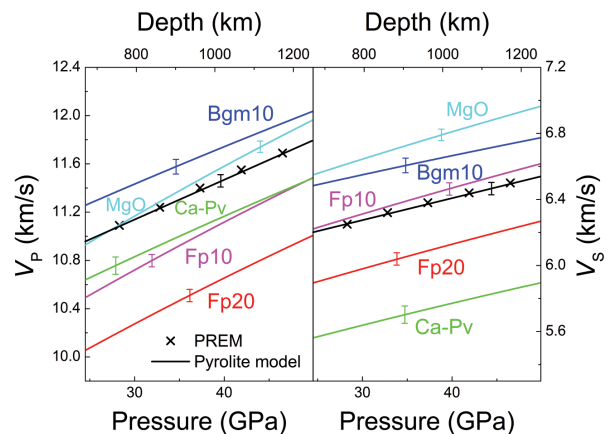

FIGURE 10. Aggregate V_P and V_S of bridgmanite, ferropericlase, and Ca-perovskite in the Earth's lower mantle. These results are compared with the PREM model (Dziewonski and Anderson 1981). For the pyrolite mineralogical model, we used 75 vol% Bgm10 (Chantel et al. 2012; Murakami et al. 2007), 20 vol% Fp20 (this study), and 5 vol% Ca-Pv (Kudo et al. 2012). Red line = Fp20; magenta line = Fp10; cyan line = MgO; blue line = Bgm10; green line = Ca-Pv; and crosses = PREM. Error bars represent the propagated uncertainties (±1σ). (Color online.)

gation of the compositions (75 vol% Bgm10, 20 vol% Fp20, and 5 vol% Ca-Pv) (Ringwood 1975; Irifune et al. 2010), were extremely consistent with velocity profiles of the PREM within uncertainties.

IMPLICATIONS

Seismic wave anisotropy of Fp in the Earth's lower mantle

Seismic studies of the Earth's mantle have reported seismic anisotropy that could result from the crystallographic lattice pre-ferred orientation (CPO) of the constituent minerals with velocity anisotropy (Blackman and Kendall 2002; Nippress et al. 2004; Niu and Perez 2004; Karato et al. 2008; Marquardt et al. 2009b; Marquardt and Morales 2012; Walpole et al. 2017). The CPO of the constituent minerals could develop due to mantle convection (Karato 1998; Tackley 2000; Long and Becker 2010; Boneh and Skemer 2014; Mainprice 2015). Therefore, understanding the seismic anisotropy of the Earth's lower mantle can greatly help us understand the geodynamics of the deep Earth (Mainprice et al. 2000; Long and Becker 2010; Romanowicz and Wenk 2017). Specifically, the viscosity of Fp seems to be pressure-dependent (Marquardt and Miyagi 2015), but Fp is still among the weak-est rheological phases in the lower mantle and can significantly contribute to the seismic anisotropy of the lower mantle (e.g., Marquardt et al. 2009b; Miyagi and Wenk 2016; Immoor et al. 2018). The elastic anisotropy of Fp combined with its rheological weakness can play a significant role in the interpretation of the observed seismic anisotropy in the lower mantle (e.g., Yamazaki and Karato 2001; Yamazaki et al. 2009; Marquardt and Miyagi 2015; Girard et al. 2016).

To decipher the potential influence of Fp on the lower-mantle seismic anisotropy, we calculated the AV_P and AV_S of Fp10 and Fp20 along a representative geotherm using the aforementioned thermoelastic modeling method (Fig. 11). At a 670 km depth, the AV_P and AV_S of Fp20 are 3.7% and 8.86%, respectively, and the dif-ference between the vertically V_{SV} and horizontally V_{SH} polarized shear waves is 0.45 km/s. The AV_P and AV_S of Fp10 are 4.4% and 9.87%, respectively, and the difference between the orthogonally polarized shear waves V_{SV} and V_{SH} is 0.55 km/s. However, at a depth of ~1250 km, the AV_P is 5.0%, AV_S is 11.42% for Fp20, and the difference between V_{SH} and V_{SV} is 0.66 km/s. The AV_P is 3.7% and AV_S is 8.09% for Fp10, and the difference between V_{SH} and V_{SV} is 0.51 km/s. These results showed that Fp was clearly V_P and V_S anisotropic in the upper regions of the lower mantle and both the increase of Fe content in Fp and the increasing depth from 670 to 1250 km could change the V_P and V_S anisotropies of Fp. We should caution that the extrapolated velocity anisotropies were only for the high-spin Fp, and did not take the potential spin transition effects on the elasticity into account. The spin transition of iron has been reported to significantly enhance the elastic shear anisotropy of Fp at high pressure and room temperature (Marquardt et al. 2009b; Yang et al. 2015), making low-spin Fp much more anisotropic than Bgm (the most abundant lower mantle mineral) in the deeper parts of the lower mantle.

Origins of seismic lateral heterogeneities at the Earth's lower mantle

Seismic lateral heterogeneities have been detected in the lower mantle (e.g., van der Hilst and Kárason 1999; Masters et al. 2000;
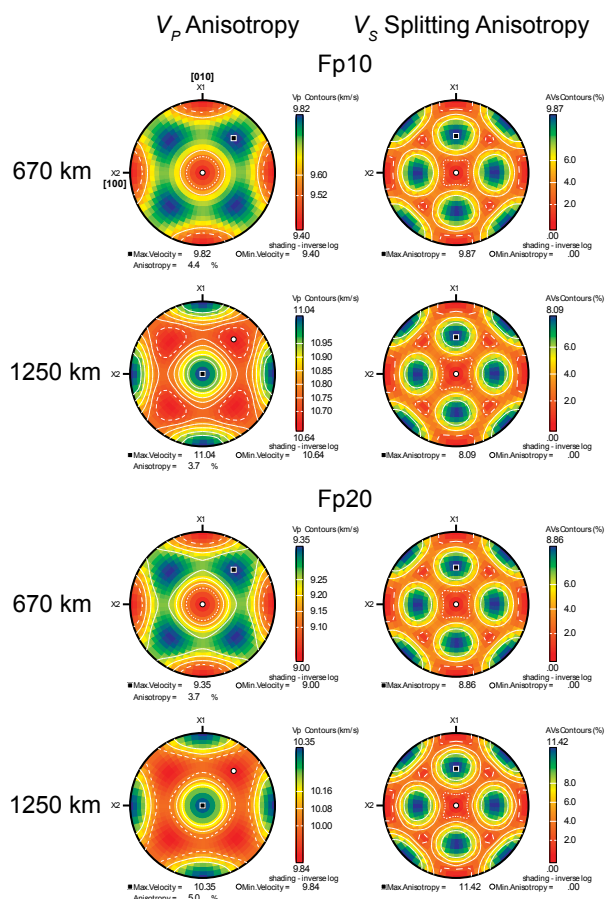

FIGURE 11. Upper hemisphere pole figures of the V_P anisotropy and V_S splitting anisotropy of Fp10 and Fp20 at 670 and 1250 km, respectively. Calculations were performed using the petrophysical software UnicefCareware of Mainprice (1990) with the modeled single-crystal elastic moduli from this study. (Color online.)

Karato and Karki 2001; Li 2009; Wu and Wentzcovitch 2017; Schumacher et al. 2018). However, their interpretation is still uncertain. While some studies have suggested that the seismic heterogeneities of the lower mantle was mainly due to thermal effects (e.g., Forte et al. 1994; Forte 2000; Simmons et al. 2010), many other studies have suggested chemically induced heteroge-neities (e.g., Antolik et al. 2003; Resovsky and Trampert 2003; Garnero and McNamara 2008; Kaneshima and Helffrich 2010; Mosca et al. 2012; Koelemeijer et al. 2016). Distinguishing the thermal or chemical origin of the seismic heterogeneities in the lower mantle is crucial because each origin has a drastically dif-ferent consequence and affects our understanding of the Earth's interior dynamic (Karato and Karki 2001). Experimental elasticity studies of the major minerals in the lower mantle (such as Fp) at relevant high P-T conditions play a significant role in understand-ing the seismic signatures, and also provide a new constraint on the seismic structures and evolution of the lower mantle (Karato and Karki 2001; Yang et al. 2016).

The thermal or chemical origins of the seismic lateral heteroge-neities can be constrained by comparing the observed ratios of vari-

ous seismic parameters with mineral physics results (e.g., Karato and Karki 2001; Wu and Wentzcovitch 2014; Yang et al. 2016). To investigate the thermal variation of the heterogeneities ratios ($R_{S/P} = \partial \ln V_S / \partial \ln V_P$) for Fp, we calculated the thermally induced variations in V_S and V_P for MgO, Fp10, and Fp20 (Fig. 12a). In the modeling, the velocities of these phases were first extrapolated along a representative geotherm (Katsura et al. 2010) based on the derived thermoelastic parameters and finite-strain theory. In addition, we applied a positive and negative temperature perturbation of 200 K to the velocities to determine the $\partial \ln V_S / \partial T$ and $\partial \ln V_P / \partial T$ for Fp. The $R_{S/P}$ values of MgO, Fp10, and Fp20 show an increase of ~2–5% from 670 to 1250 km, indicating that high temperature increases the $R_{S/P}$ value of Fp. The $R_{S/P}$ profile of Fp20 is ~30% and ~50% higher than Fp10 and MgO, respectively. Therefore, our results showed that the thermally induced $R_{S/P}$ was sensitive to composition and the FeO content had a significant increasing effect on the thermally induced $R_{S/P}$ of Fp in the upper part of the lower mantle. This also agrees with a previous theoretical prediction, which showed that compositional variations could change the thermally induced $R_{S/P}$ depth profiles in the lower mantle (Wu and Wentzcovitch 2017).

The amount of FeO in the Earth's lower mantle minerals is particularly important because it can affect a wide range of elastic properties, including their densities, sound velocities, bulk moduli, and shear moduli (Jacobsen et al. 2002; Yang et al. 2015). Previous studies have also suggested that the variation of FeO content

in Fp may be regarded as a potential chemical cause for seismic lateral heterogeneities (van der Hilst and Kárason 1999). Here, we also calculated the Fe-induced variations of V_S and V_P for Fp (MgO, Fp10, and Fp20) from 670 to 1250 km along a representative geotherm (Fig. 12b). Due to change of the Fe content in Fp, the value of $R_{S/P}$ shows a distinctly increasing trend from ~1.92 at 670 km to ~2.21 at 1250 km (Fig. 12b), which is similar with the upward trending thermally induced variation of Fp (MgO, Fp10, and Fp20) but has significantly steeper slopes. These results indicate that the value of $R_{S/P}$ distinctly increases with increasing Fe content in Fp. Specifically, the value of $R_{S/P}$ due to change of the Fe content (Fe-induced variation) in Fp is ~45 and ~20% higher than the thermally induced variation of MgO and Fp10, respectively. The value of $R_{S/P}$ due to change of the Fe content in Fp is ~10% lower than the thermally induced variation of Fp20. Moreover, our value of $R_{S/P}$ due to change of the Fe content in Fp is also ~15% higher than the one from a previous study by Yang et al. (2016) (dot-dashed line in Fig. 12b) within their uncertainties. There are two possible reasons for the slightly different results between this study and Yang et al. (2016). One of them is that we calculated the Fe-induced variations of V_S and V_P for Fp with up to 20 mol% FeO, whereas Yang et al. (2016) only limited Fp with up to 10 mol% FeO. Another reason is that Yang et al. (2016) calculated the relative variations of velocity with a Fe content using the high-pressure and room-temperature elasticity data of MgO (Sinogeikin and Bass 2000) as their benchmark data. These factors clearly highlight the importance of our current simultaneously high P-T elasticity studies of MgO.

In addition, even though some seismic studies showed a decreasing trend of $R_{S/P}$ in the upper part of the lower mantle (e.g., Mosca et al. 2012), most seismic studies demonstrated an increasing trend in the same depth region, where the $R_{S/P}$ was ~1.7 at the top of the lower mantle and ~2.0 in the mid-lower mantle (e.g., Robertson and Woodhouse 1996; Romanowicz 2001; Simmons et al. 2010). Compared to the seismic observation results (dashed lines in Fig. 12b), the $R_{S/P}$ value of the thermally induced variation for Fp10 is consistent with most seismic observations within uncertainty. However, the thermally induced $R_{S/P}$ value of Fp20, which is the relevant composition of Fp in the lower mantle, is ~50% higher than most seismic observations within uncertainty for the upper part of the lower mantle (e.g., Robertson and Woodhouse 1996; Romanowicz 2001; Houser et al. 2008; Simmons et al. 2010; Mosca et al. 2012; Koelemeijer et al. 2016). On the contrary, the value of $R_{S/P}$ due to change of the Fe content in Fp is relatively consistent with some seismic observations within uncertainty in the upper part of the lower mantle (e.g., Robertson and Woodhouse 1996; Romanowicz 2001; Simmons et al. 2010). Thus, based on the results for Fp in this study, we propose that the Fe-induced heterogeneities can offer a significant contribution to the observed seismic lateral heterogeneities in the lower mantle. This also agrees with the results of seismology studies, which showed that the seismic heterogeneities in the lower mantle could not be explained by thermal anomalies alone, and suggested the presence of chemical heterogeneities, might be a local variation of Fe content, as an alternative explanation (e.g., Kellogg et al. 1999; van der Hilst and Kárason 1999; Wysession et al. 1999; Houser et al. 2008). We should note that the above mentioned Fe-induced heterogeneities in the lower mantle did not take the potential contributions from
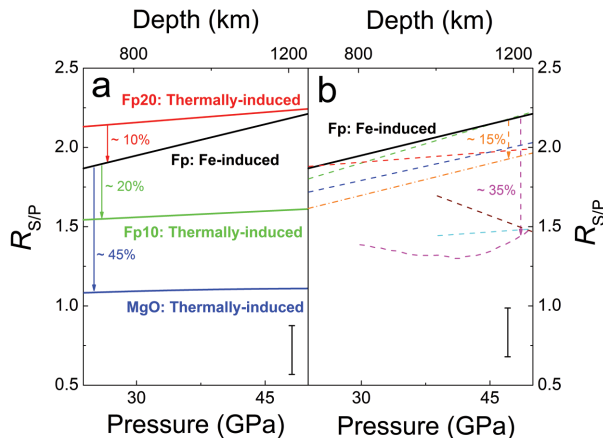

Figure 12. Depth profile of the thermally induced (**a**) and Fe-induced (**b**) heterogeneities ratios ($R_{S/P} = \partial \ln V_S / \partial \ln V_P$) for Fp along a representative geotherm (Katsura et al. 2010). (**a**) Solid blue line = thermal-induced heterogeneities ratio of MgO; solid green line = thermal-induced heterogeneities ratio of Fp10; solid red line = thermal-induced heterogeneities ratio of Fp20. (**b**) Solid black line = Fe-induced heterogeneities ratio of Fp; and orange dot-dashed line = Fe-induced heterogeneities ratio of Fp6 (Yang et al. 2016). Seismic models are also shown as a dashed line. Magenta dashed line = SP12RTS (Koelemeijer et al. 2016); cyan dashed line = HMSL08 (Houser et al. 2008); wine dashed line = MCDRT12 (Mosca et al. 2012); red dashed line = GyPSuM (Simmons et al. 2010); blue dashed line = RW96 (Robertson and Woodhouse 1996); and green dashed line = RB01 (Romanowicz 2001). The representative error bars (standard deviation, ±1σ) are estimated using the standard error propagation from the modeled parameters. Vertical lines with arrows represent the differences in percentage for the $R_{S/P}$ ratios. (Color online.)

Bgm into account because Fe preferentially partitions into Fp in the lower mantle (e.g., Auzende et al. 2008; Sakai et al. 2009; Muir and Brodholt 2016; Kaminsky and Lin 2017; Xu et al. 2017), and there are few single-crystal elasticity experimental studies of Bgm at high *P-T* conditions (e.g., Sinogeikin et al. 2004b). Future single-crystal elasticity studies of Fp and Bgm at the relevant *P-T* and compositional (the possible Fp and Bgm compositions expected in the lower mantle) conditions are needed to provide a more comprehensive understanding of the seismic anisotropy and lateral heterogeneities of the Earth's lower mantle.

REFERENCES CITED

Andrault, D. (2001) Evaluation of (Mg,Fe) partitioning between silicate perovskite and magnesiowüstite up to 120 GPa and 2300 K. Journal of Geophysical Research, 106(B2), 2079–2087.

Antolik, M., Gu, Y.J., Ekström, G., and Dziewonski, A.M. (2003) J362D28: a new joint model of compressional and shear velocity in the Earth's mantle. Geophysical Journal International, 153(2), 443–466.

Antonangeli, D., Siebert, J., Aracne, C.M., Farber, D.L., Bosak, A., Hoesch, M., Krisch, M., Ryerson, F.J., Fiquet, G., and Badro, J. (2011) Spin crossover in ferropericlase at high pressure: A seismologically transparent transition? Science, 331, 64–67.

Auzende, A.L., Badro, J., Ryerson, F.J., Weber, P.K., Fallon, S.J., Addad, A., Siebert, J., and Fiquet, G. (2008) Element partitioning between magnesium silicate perovskite and ferropericlase: New insights into bulk lower-mantle geochemistry. Earth and Planetary Science Letters, 269(1-2), 164–174.

Badro, J., Fiquet, G., Guyot, F., Rueff, J.P., Struzhkin, V.V., Vanko, G., and Monaco, G. (2003) Iron partitioning in Earth's mantle: Toward a deep lower mantle discontinuity. Science, 300(5620), 789–791.

Belonoshko, A.B., Arapan, S., Martonak, R., and Rosengren, A. (2010) MgO phase diagram from first principles in a wide pressure-temperature range. Physical Review B, 81(5), 054110.

Birch, F. (1978) Finite strain isotherm and velocities for single-crystal and polycrystal-line NaCl at high pressure and 300 K. Journal of Geophysical Research, 83(B3), 1257–1268.

Blackman, D.K., and Kendall, J.M. (2002) Seismic anisotropy in the upper mantle 2. Predictions for current plate boundary flow models. Geochemistry, Geophysics, Geosystems, 3(9), 8602.

Bolis, R.M., Morard, G., Vinci, T., Ravasio, A., Bambrink, E., Guarguaglini, M., Koenig, M., Musella, R., Remus, F., Bouchet, J., and others. (2016) Decaying shock studies of phase transitions in MgO-SiO₂ systems: Implications for the super-Earths' interiors. Geophysical Research Letters, 43(18), 9475–9483.

Boneh, Y., and Skemer, P. (2014) The effect of deformation history on the evolution of olivine CPO. Earth and Planetary Science Letters, 406, 213–222.

Chantel, J., Frost, D.J., McCammon, C.A., Jing, Z.C., and Wang, Y.B. (2012) Acoustic velocities of pure and iron-bearing magnesium silicate perovskite measured to 25 GPa and 1200 K. Geophysical Research Letters, 39(19), L19307.

Chen, G.L., Liebermann, R.C., and Weidner, D.J. (1998) Elasticity of single-crystal MgO to 8 gigapascals and 1600 Kelvin. Science, 280, 1913–1916.

Coppari, F., Smith, R.F., Eggert, J.H., Wang, J., Rygg, J.R., Lazicki, A., Hawreliak, J.A., Collins, G.W., and Duffy, T.S. (2013) Experimental evidence for a phase transition in magnesium oxide at exoplanet pressures. Nature Geoscience, 6, 926–929.

Crowhurst, J.C., Brown, J.M., Goncharov, A.F., and Jacobsen, S.D. (2008) Elasticity of (Mg,Fe)O through the spin transition of iron in the lower mantle. Science, 319, 451–453.

Dewaele, A., Fiquet, G., Andrault, D., and Hausermann, D. (2000) P-V-T equation of state of periclase from synchrotron radiation measurements. Journal of Geophysical Research, 105(B2), 2869–2877.

Dorfman, S.M., Prakapenka, V.B., Meng, Y., and Duffy, T.S. (2012) Intercomparison of pressure standards (Au, Pt, Mo, MgO, NaCl, and Ne) to 2.5 Mbar. Journal of Geophysical Research, 117(B8), B08210.

Dorogokupets, P.I. (2010) P-V-T equations of state of MgO and thermodynamics. Physics and Chemistry of Minerals, 37(9), 677–684.

Duan, Y.F., Li, X.Y., Sun, N.Y., Ni, H.W., Tkachev, S.N., and Mao, Z. (2018) Single-crystal elasticity of MgAl₂O₄-spinel up to 10.9 GPa and 1000 K: Implication for the velocity structure of the top upper mantle. Earth and Planetary Science Letters, 481, 41–47.

Duffy, T.S., and Ahrens, T.J. (1995) Compressional sound velocity, equation of state, and constitutive response of shock-compressed magnesium oxide. Journal of Geophysical Research, 100(B1), 529–542.

Duffy, T.S., and Anderson, D.L. (1989) Seismic velocities in mantle minerals and the mineralogy of the upper mantle. Journal of Geophysical Research, 94(B2), 1895–1912.

Duffy, T.S., Hemley, R.J., and Mao, H.K. (1995a) Equation of state and shear strength at multimegabar pressures: Magnesium oxide to 227 GPa. Physical Review Letters, 74(8), 1371–1374.

Duffy, T.S., Zha, C.S., Downs, R.T., Mao, H.K., and Hemley, R.J. (1995b) Elasticity of forsterite to 16 GPa and the composition of the upper mantle. Nature, 378, 170–173.

Duffy, T.S., Madhusudhan, N., and Lee, K.K.M. (2015) Mineralogy of Super-Earth Planets. In G. Schubert, Eds., Treatise on Geophysics, 2nd ed., vol. 2, p.149–178. Elsevier.

Dziewonski, A.M., and Anderson, D.L. (1981) Preliminary reference Earth model. Physics of the Earth and Planetary Interiors, 25(4), 297–356.

Every, A. (1980) General closed-form expressions for acoustic waves in elastically anisotropic solids. Physical Review B, 22(4), 1746.

Fan, D.W., Mao, Z., Yang, J., and Lin, J.F. (2015) Determination of the full elastic tensor of single crystals using shear wave velocities by Brillouin spectroscopy. American Mineralogist, 100, 2590–2601.

Fei, Y.W. (1999) Effects of temperature and composition on the bulk modulus of (Mg,Fe)O. American Mineralogist, 84, 272–276.

Fei, Y.W., Ricolleau, A., Frank, M., Mibe, K., Shen, G.Y., and Prakapenka, V.B. (2007) Towards an internally consistent pressure scale. Proceedings of the National Academy of Sciences, 104(22), 9182–9186.

Fiquet, G., Badro, J., Guyot, F., Bellin, Ch., Krisch, M., Antonangeli, D., Requardt, H., Mermet, A., Farber, D., Aracne-Ruddle, C., and Zhang, J. (2004) Application of inelastic X-ray scattering to the measurements of acoustic wave velocities in geophysical materials at very high pressure. Physics of the Earth and Planetary Interiors, 143-144, 5–18.

Forte, A.M. (2000) Seismic-geodynamic constraints on mantle flow: Implications for layered convection, mantle viscosity, and seismic anisotropy in the deep mantle. In S.I. Karato, A. Forte, R.C. Liebermann, G. Masters, and L. Stixrude, Eds., Earth's Deep Interior: Mineral Physics and Tomography from the Atomic to the Global Scale, Geophysical Monograph Series, vol. 177, pp. 441–477. American Geophysical Union, Washington, DC.

Forte, A.M., Woodward, R.L., and Dziewonski, A.M. (1994) Joint inversions of seismic and geodynamic data for models of three-dimensional mantle heterogeneities. Journal of Geophysical Research, 99(B11), 21857–21877.

Fu, S.Y., Yang, J., and Lin, J.F. (2017) Abnormal elasticity of single-crystal magnesiosiderite across the spin transition in Earth's lower mantle. Physical Review Letters, 118(3), 036402.

Garnero, E.J., and McNamara, A.K. (2008) Structure and dynamics of Earth's lower mantle. Science, 320, 626–628.

Girard, J., Amulele, G., Farla, R., Mohiuddin, A., and Karato, S.-I. (2016) Shear deformation of bridgmanite and magnesiowüstite aggregates at lower mantle conditions. Science, 351, 144–147.

Grimsditch, M. (2001) Brillouin scattering. In M. Levy, H. Bass, R. Stern, and V. Keppens, Eds., Handbook of Elastic Properties of Solids, Liquids, and Gases, p. 331–347, Academic Press.

Hill, R. (1952) The elastic behaviour of a crystalline aggregate. Proceedings of the Physical Society-Section A, 65(5), 349–354.

Houser, C., Masters, G., Shearer, P., and Laske, G. (2008) Shear and compressional velocity models of the mantle from cluster analysis of long-period waveforms. Geophysical Journal International, 174(1), 195–212.

Immoor, J., Marquardt, H., Miyagi, L., Lin, F., Speziale, S., Merkel, S., Buchen, J., Kurnosov, A., and Liermann, H.-P. (2018) Evidence for {100}<011> slip in ferropericlase in Earth's lower mantle from high-pressure/high-temperature experiments. Earth and Planetary Science Letters, 489, 251–257.

Irifune, T. (1994) Absence of an aluminous phase in the upper part of the Earth's lower mantle. Nature, 370, 131–133.

Irifune, T., Shinmei, T., McCammon, C.A., Miyajima, N., Rubie, D.C., and Frost, D.J. (2010) Iron partitioning and density changes of pyrolite in Earth's lower mantle. Science, 327, 193–195.

Isaak, D.G., Anderson, O.L., and Goto, T. (1989) Measured elastic moduli of single-crystal MgO up to 1800 K. Physics and Chemistry of Minerals, 16(7), 704–713.

Isaak, D.G., Cohen, R.E., and Mehl, M.J. (1990) Calculated elastic and thermal properties of MgO at high pressures and temperatures. Journal of Geophysical Research,

95(B5), 7055–7067.

Ito, E., Kubo, A., Katsura, T., and Walter, M.J. (2004) Melting experiments of mantle materials under lower mantle conditions with implications for magma ocean differentiation. Physics of the Earth and Planetary Interiors, 143-144, 397–406.

Jackson, I., and Niesler, H. (1982) The elasticity of periclase to 3 GPa and some geophysical implications. In S. Akimoto and M.H. Manghnani, Eds., High Pressure Research in Geophysics, pp. 93–113. Center for Academic Publications Japan, Tokyo.

Jackson, J.M., Sinogeikin, S.V., Jacobsen, S.D., Reichmann, H.J., Mackwell, S.J., and Bass, J.D. (2006) Single-crystal elasticity and sound velocities of $(Mg_{0.94}Fe_{0.06})O$ ferropericlase to 20 GPa. Journal of Geophysical Research, 111(B9), B09203.

Jacobsen, S.D., Reichmann, H.J., Spetzler, H.A., Mackwell, S.J., Smyth, J.R., Angel, R.J., and McCammon, C.A. (2002) Structure and elasticity of single-crystal (Mg,Fe)O and a new method of generating shear waves for gigahertz ultrasonic interferometry. Journal of Geophysical Research, 107(B2), ECV 4-1–ECV 4-14.

Jacobsen, S.D., Holl, C.M., Adams, K.A., Fischer, R.A., Martin, E.S., Bina, C.R., Lin, J.F., Prakapenka, V.B., Kubo, A., and Dera, P. (2008) Compression of single-crystal magnesium oxide to 118 GPa and a ruby pressure gauge for helium pressure media. American Mineralogist, 93, 1823–1828.

Kaminsky, F.V., and Lin, J.F. (2017) Iron partitioning in natural lower-mantle minerals: Toward a chemically heterogeneous lower mantle. American Mineralogist, 102, 824–832.

Kaneshima, S., and Helffrich, G. (2010) Small scale heterogeneities in the mid-lower mantle beneath the circum-Pacific area. Physics of the Earth and Planetary Interiors, 183(1), 91–103.

Kantor, I., Prakapenka, V., Kantor, A., Dera, P., Kurnosov, A., Sinogeikin, S., Dubrovinskaia, N., and Dubrovinsky, L. (2012) BX90: A new diamond anvil cell design for X-ray diffraction and optical measurements. Review of Scientific Instruments, 83(12), 125102.

Karato, S.I. (1998) Seismic anisotropy in the deep mantle, boundary layers and the geometry of mantle convection. Pure and Applied Geophysics, 151(2-4), 565–587.

Karato, S., and Karki, B.B. (2001) Origin of lateral variation of seismic wave velocities and density in the deep mantle. Journal of Geophysical Research, 106(B10), 21771–21783.

Karato, S.I., Jung, H., Katayama, I., and Skmer, P. (2008) Geodynamic significance of seismic anisotropy of the upper mantle: New insights from laboratory studies. Annual Review of Earth and Planetary Sciences, 36, 59–95.

Karki, B.B., Stixrude, L., Clark, S.J., Warren, M.C., Ackland, G.J., and Crain, J. (1997) Structure and elasticity of MgO at high pressure. American Mineralogist, 82, 51–60.

Karki, B.B., Wentzcovitch, R.M., Gironcoli, S., and Baroni, S. (1999) First-principles determination of elastic anisotropy and wave velocities of MgO at lower mantle conditions. Science, 286, 1705–1707.

Katsura, T., Yoneda, A., Yamazaki, D., Yoshino, T., and Ito, E. (2010) Adiabatic temperature profile in the mantle. Physics of the Earth and Planetary Interiors, 183(1-2), 212–218.

Kellogg, L.H., Hager, B.H., and van der Hilst, R.D. (1999) Compositional stratification in the deep mantle. Science, 283, 1881–1884.

Kimura, T., Ohfuji, H., Nishi, M., and Irifune, T. (2017) Melting temperature of MgO under high pressure by micro-texture analysis. Nature Communications, 8, 15735.

Koelemeijer, P., Ritsema, J., Deuss, A., and van Heijst, H.-J. (2016) SP12RTS: A degree-12 model of shear-and compressional-wave velocity for Earth's mantle. Geophysical Journal International, 204(2), 1024–1039.

Kono, Y., Irifune, T., Higo, Y., Inoue, T., and Barnhoorn, A. (2010) P-V-T relation of MgO derived by simultaneous elastic wave velocity and in situ X-ray measurements: A new pressure scale for the mantle transition region. Physics of the Earth and Planetary Interiors, 183(1-2), 196–211.

Kudo, Y., Hirose, K., Murakami, M., Asahara, Y., Ozawa, H., Ohishi, Y., and Hirao, N. (2012) Sound velocity measurements of $CaSiO_3$ perovskite to 133 GPa and implications for lowermost mantle seismic anomalies. Earth and Planetary Science Letters, 349-350, 1–7.

Kung, J., Li, B.S., Weidner, D.J., Zhang, J.Z., and Liebermann, R.C. (2002) Elasticity of $(Mg_{0.83},Fe_{0.17})O$ ferropericlase at high pressure: ultrasonic measurements in conjunction with X-radiation techniques. Earth and Planetary Science Letters, 203(1), 557–566.

Li, B.S. (2009) Characteristics of lateral heterogeneities with thermal and chemical origins in the pyrolitic lower mantle. Progress in Natural Science, 19(11), 1603–1611.

Li, B., Kung, J., Uchida, T., and Wang, Y.B. (2005) Pressure calibration to 20 GPa by simultaneous use of ultrasonic and X-ray techniques. Journal of Applied Physics, 98(1), 013521.

Li, B.S., Woody, K., and Kung, J. (2006) Elasticity of MgO to 11 GPa with an independent absolute pressure scale: Implications for pressure calibration. Journal of Geophysical Research, 111(B11), B11206.

Lin, J.F., and Tsuchiya, T. (2008) Spin transition of iron in the Earth's lower mantle. Physics of the Earth and Planetary Interiors, 170(3-4), 248–259.

Lin, J.F., Struzhkin, V.V., Jacobsen, S.D., Hu, M.Y., Chow, P., Kung, J., Liu, H., Mao, H.K., and Hemley, R.J. (2005) Spin transition of iron in magnesiowustite in the Earth's lower mantle. Nature, 436, 377–380.

Lin, J.F., Jacobsen, S.D., Sturhahn, W., Jackson, J.M., Zhao, J.C., and Yoo, C.S. (2006) Sound velocities of ferropericlase in the Earth's lower mantle. Geophysical Research Letters, 33(22), L22304.

Lin, J.F., Speziale, S., Mao, Z., and Marquardt, H. (2013) Effects of the electronic spin transitions of iron in lower-mantle minerals: Implications to deep-mantle geophysics and geochemistry. Reviews of Geophysics, 51(2), 244–275.

Long, M.D., and Becker, T.W. (2010) Mantle dynamics and seismic anisotropy. Earth and Planetary Science Letters, 297, 341–354.

Lu, C., Mao, Z., Lin, J.F., Zhuravlev, K.K., Tkachev, S.N., and Prakapenka, V.B. (2013) Elasticity of single-crystal iron-bearing pyrope up to 20 GPa and 750 K. Earth and Planetary Science Letters, 361, 134–142.

Mainprice, D. (1990) A Fortran program to calculate seismic anisotropy from the lattice preferred orientation of minerals. Computers & Geosciences, 16(3), 385–393.

——— (2015) Seismic anisotropy of the deep earth from a mineral and rock physics perspective. In G. Schubert, Eds., Treatise on Geophysics, 2nd ed., vol. 2, p. 487–538. Elsevier.

Mainprice, D., Barruol, G., and Ben Ismail, W. (2000) The anisotropy of the Earth's mantle: From single crystal to polycrystal. In S.I. Karato, L. Stixrude, R. Liebermann, G. Masters, and A. Forte, Eds., Mineral Physics and Seismic Tomography from the Atomic to the Global Scale, Geophysical Monograph Series, vol. 177, p. 237–264. American Geophysical Union, Washington, D.C.

Mao, H.K., Xu, J., and Bell, P.M. (1986) Calibration of the ruby pressure gauge to 800 kbar under quasi-hydrostatic conditions. Journal of Geophysical Research, 91(B5), 4673–4676.

Mao, H.K., Shen, G.Y., and Hemley, R.J. (1997) Multivariable dependence of Fe-Mg partitioning in the lower mantle. Science, 278, 2098–2100.

Mao, Z., Lin, J.F., Jacobsen, S.D., Duffy, T.S., Chang, Y.Y., Smyth, J.R., Frost, D.J., Hauri, E.H., and Prakapenka, V.B. (2012) Sound velocities of hydrous ringwoodite to 16 GPa and 673 K. Earth and Planetary Science Letters, 331-332, 112–119.

Mao, Z., Fan, D.W., Lin, J.F., Yang, J., Tkachev, S.N., Zhuravlev, K., and Prakapenka, V.B. (2015) Elasticity of single-crystal olivine at high pressures and temperatures. Earth and Planetary Science Letters, 426, 204–215.

Marquardt, H., and Miyagi, L. (2015) Slab stagnation in the shallow lower mantle linked to an increase in mantle viscosity. Nature Geoscience, 8(4), 311–314.

Marquardt, H., and Morales, L. (2012) Ferropericlase layering as potential cause for seismic anisotropy in Earth's lower mantle? European Mineralogical Conference, 1, EMC2012-562.

Marquardt, H., Speziale, S., Reichmann, H.J., Frost, D.J., and Schilling, F.R. (2009a) Single-crystal elasticity of $(Mg_{0.9}Fe_{0.1})O$ to 81 GPa. Earth and Planetary Science Letters, 287(3-4), 345–352.

Marquardt, H., Speziale, S., Reichmann, H.J., Frost, D.J., Schilling, F.R., and Garnero, E.J. (2009b) Elastic shear anisotropy of ferropericlase in Earth's lower mantle. Science, 324, 224–226.

Masters, G., Laske, G., Bolton, H., and Dziewonski, A. (2000) The relative behavior of shear velocity, bulk sound speed, and compressional velocity in the mantle: Implications for chemical and thermal structure. In S.I. Karato, L. Stixrude, R. Liebermann, G. Masters, and A. Forte, Eds., Mineral Physics and Seismic Tomography from the Atomic to the Global Scale, Geophysical Monograph Series, vol. 177, p. 63–87. American Geophysical Union, Washington, D.C.

Matsui, M., Parker, S.C., and Leslie, M. (2000) The MD simulation of the equation of state of MgO: Application as a pressure calibration standard at high temperature and high pressure. American Mineralogist, 85, 312–316.

Mattern, E., Matas, J., Ricard, Y., Bass, J.D. (2005) Lower mantle composition and temperature from mineral physics and thermodynamic modeling. Geophysical Journal International, 160(3), 973–990.

McWilliams, R.S., Spaulding, D.K., Eggert, J.H., Celliers, P.M., Hicks, D.G., Smith, R.F., Collins, G.W., and Jeanloz, R. (2012) Phase transformations and metallization of magnesium oxide at high pressure and temperature. Science, 338, 1330–1333.

Miyagi, L., and Wenk, H.-R. (2016) Texture development and slip systems in bridgmanite and bridgmanite+ferropericlase aggregates. Physics and Chemistry of Minerals, 43(8), 597–613.

Mosca, I., Cobden, L., Deuss, A., Ritsema, J., and Trampert, J. (2012) Seismic and mineralogical structures of the lower mantle from probabilistic tomography. Journal of Geophysical Research, 117(B6), B06304.

Muir, J.M.R., and Brodholt, J.P. (2015) Elastic properties of ferropericlase at lower mantle conditions and its relevance to ULVZs. Earth and Planetary Science Letters, 417, 40–48.

——— (2016) Ferrous iron partitioning in the lower mantle. Physics of the Earth and Planetary Interiors, 257, 12–17.

Murakami, M., Sinogeikin, S.V., Hellwig, H., Bass, J.D., and Li, J. (2007) Sound velocity of $MgSiO_3$ perovskite to Mbar pressure. Earth and Planetary Science Letters, 256(1-2), 47–54.

Murakami, M., Ohishi, Y., Hirao, N., and Hirose, K. (2009) Elasticity of MgO to 130 GPa: Implications for lower mantle mineralogy. Earth and Planetary Science Letters, 277(1-2), 123–129.

——— (2012) A perovskitic lower mantle inferred from high-pressure, high-temperature sound velocity data. Nature, 485, 90–94.

Nippress, S.E.J., Kusznir, N.J., and Kendall, J.M. (2004) Modeling of lower mantle seismic anisotropy beneath subduction zones. Geophysical Research Letters, 31(19), L19612.

Niu, F.L., and Perez, A.M. (2004) Seismic anisotropy in the lower mantle: A comparison of waveform splitting of SKS and SKKS. Geophysical Research Letters, 31(24), L24612.

Oganov, A.R., Gillan, M.J., and Price, G.D. (2003) Ab initio lattice dynamics and struc-

tural stability of MgO. The Journal of Chemical Physics, 118(22), 10174–10182.

Ostwald, J., Pazold, W., and Weis, O. (1977) High-resolution Brillouin spectroscopy of water. Applied Physics, 13(4), 351–356.

Polian, A., Vo-Thanh, D., and Richet, P. (2002) Elastic properties of α-SiO$_2$ up to 2300 K from Brillouin scattering measurements. Europhysics Letters, 57(3), 375–381.

Reichmann, H.J., Angel, R.J., Spetzler, H., and Bassett, W.A. (1998) Ultrasonic interferometry and X-ray measurements on MgO in a new diamond anvil cell. American Mineralogist, 83, 1357–1360.

Reichmann, H.J., Sinogeikin, S.V., and Bass, J.D. (2008) Single-crystal elastic properties of (Mg$_{0.987}$,Fe$_{0.013}$)O to 9 GPa. American Mineralogist, 93, 1306–1311.

Resovsky, J., and Trampert, J. (2003) Using probabilistic seismic tomography to test mantle velocity–density relationships. Earth and Planetary Science Letters, 215(1-2), 121–134.

Ricolleau, A., Fei, Y.W., Cottrell, E., Watson, H., Deng, L.W., Zhang, L., Fiquet, G., Auzende, A.-L., Roskosz, M., Morard, G., and Prakapenka, V. (2009) Density profile of pyrolite under the lower mantle conditions. Geophysical Research Letters, 36(6), L06302.

Ringwood, A.E. (1975) Composition and Petrology of the Earth's Mantle. McGraw-Hill, New York.

Robertson, G.S., and Woodhouse, J.H. (1996) Ratio of relative S to P velocity heterogeneities in the lower mantle. Journal of Geophysical Research, 101(B9), 20,041–20,052.

Romanowicz, B. (2001) Can we resolve 3D density heterogeneities in the lower mantle? Geophysical Research Letters, 28(6), 1107–1110.

Romanowicz, B., and Wenk, H.-R. (2017) Anisotropy in the deep Earth. Physics of the Earth and Planetary Interiors, 269, 58–90.

Sakai, T., Ohtani, E., Terasaki, H., Sawada, N., Kobayashi, Y., Miyahara, M., Nishijima, M., Hirao, N., Ohishi, Y., and Kikegawa, T. (2009) Fe-Mg partitioning between perovskite and ferropericlase in the lower mantle. American Mineralogist, 94, 921–925.

Sandercock, J.R. (1982) Trends in Brillouin scattering: studies of opaque materials, supported films, and central modes. In M. Cardona and J. Guntherodt, Eds., Topics in Applied Physics, p. 173–206. Springer-Verlag, Berlin.

Sang, L.Q., and Bass, J.D. (2014) Single-crystal elasticity of diopside to 14 GPa by Brillouin scattering. Physics of the Earth and Planetary Interiors, 228, 75–79.

Schumacher, L., Thomas, C., and Abreu, R. (2018) Out-of-plane seismic reflections beneath the Pacific and their geophysical implications. Journal of Geophysical Research, 123(3), 2286–2302.

Simmons, N.A., Forte, A.M., Boschi, L., and Grand, S.P. (2010) GyPSuM: A joint tomographic model of mantle density and seismic wave speeds. Journal of Geophysical Research, 115(B12), B12310.

Sinogeikin, S.V., and Bass, J.D. (2000) Single-crystal elasticity of pyrope and MgO to 20 GPa by Brillouin scattering in the diamond cell. Physics of the Earth and Planetary Interiors, 120(1-2), 43–62.

——— (2002) Elasticity of majorite and a majorite-pyrope solid solution to high pressure: implications for the transition zone. Geophysical Research Letters, 29(2), 1017.

Sinogeikin, S.V., Jackson, J.M., O'Neill, B., Palko, J.W., and Bass, J.D. (2000) Compact high-temperature cell for Brillouin scattering measurements. Review of Scientific Instruments, 71(1), 201–206.

Sinogeikin, S.V., Lakshtanov, D.L., Nicholas, J.D., and Bass, J.D. (2004a) Sound velocity measurements on laser-heated MgO and Al$_2$O$_3$. Physics of the Earth and Planetary Interiors, 143-144, 575–586.

Sinogeikin, S.V., Zhang, J.Z., and Bass, J.D. (2004b) Elasticity of single crystal and polycrystalline MgSiO$_3$ perovskite by Brillouin spectroscopy. Geophysical Research Letters, 31(6), L06620.

Sinogeikin, S.V., Bass, J.D., Prakapenka, V., Lakshtanov, D., Shen, G., Sanchez-Valle, C., and Rivers, M. (2006) Brillouin spectrometer interfaced with synchrotron radiation for simultaneous X-ray density and acoustic velocity measurements. Review of Scientific Instruments, 77(10), 103905.

Speziale, S., Marquardt, H., and Duffy, T.S. (2014) Brillouin scattering and its application in geosciences. Reviews in Mineralogy and Geochemistry, 78, 543–603.

Speziale, S., Zha, C.S., Duffy, T.S., Hemley, R.J., and Mao, H.K. (2001) Quasi-hydrostatic compression of magnesium oxide to 52 GPa: Implications for the pressure-volume-temperature equation of state. Journal of Geophysical Research, 106(B1), 515–528.

Sumino, Y., Anderson, O.L., and Suzuki, I. (1983) Temperature coefficients of elastic constants of single crystal MgO between 80 and 1300 K. Physics and Chemistry of Minerals, 9(1), 38–47.

Tackley, P.J. (2000) Mantle convection and plate tectonics: Toward an integrated physical and chemical theory. Science, 288, 2002–2007.

Tange, Y., Nishihara, Y., and Tsuchiya, T. (2009) Unified analyses for P-V-T equation of state of MgO: A solution for pressure-scale problems in high P-T experiments. Journal of Geophysical Research, 114(B3), B03208.

Tateno, S., Hirose, K., and Ohishi, Y. (2014) Melting experiments on peridotite to lowermost mantle conditions. Journal of Geophysical Research, 119(6), 4684–4694.

Tsuchiya, T., Wentzcovitch, R.M., da Silva, C.R.S., and de Gironcoli, S. (2006) Spin transition in magnesiowustite in Earth's lower mantle. Physical Review Letters, 96(19), 198501.

Utsumi, W., Weidner, D.J., and Lieberman, R.C. (1998) Volume measurement of MgO at high pressures and temperatures. In M.H. Manghnani and T. Yagi, Eds., Properties of Earth and Planetary Materials at High Pressure and Temperature, Geophysical Monograph Series, vol. 101, p. 327–333. American Geophysical Union, Washington, D.C.

van der Hilst, R.D., and Kárason, H. (1999) Compositional heterogeneities in the bottom 1000 kilometers of Earth's mantle: Toward a hybrid convection model. Science, 283(5409), 1885–1888.

Walpole, J., Wookey, J., Kendall, J.M., and Masters, T.G. (2017) Seismic anisotropy and mantle flow below subducting slabs. Earth and Planetary Science Letters, 465, 155–167.

Wentzcovitch, R.M., Justo, J.F., Wu, Z.Q., da Silva, C.R.S., Yuen, D.A., and Kohlstedt, D. (2009) Anomalous compressibility of ferropericlase throughout the iron spin cross-over. Proceedings of the National Academy of Sciences, 106(21), 8447–8452.

Wood, B.J. (2000) Phase transformations and partitioning relations in peridotite under lower mantle conditions. Earth and Planetary Science Letters, 174(3-4), 341–354.

Wu, Z.Q., and Wentzcovitch, R.M. (2014) Spin crossover in ferropericlase and velocity heterogeneities in the lower mantle. Proceedings of the National Academy of Sciences, 111(29), 10468–10472.

——— (2017) Composition versus temperature induced velocity heterogeneities in a pyrolitic lower mantle. Earth and Planetary Science Letters, 457, 359–365.

Wu, Z.Q., Wentzcovitch, R.M., Umemoto, K., Li, B.S., Hirose, K., and Zheng, J.C. (2008) Pressure-volume-temperature relations in MgO: An ultrahigh pressure-temperature scale for planetary sciences applications. Journal of Geophysical Research, 113(B6), B06204.

Wu, Z.Q., Justo, J.F., da Silva, C.R.S., de Gironcoli, S., and Wentzcovitch, R.M. (2009) Anomalous thermodynamic properties in ferropericlase throughout its spin crossover. Physical Review B, 80(1), 014409.

Wu, Y., Yang, J., Wu, X., Song, M.S., Yoshino, T., Zhai, S.M., Qin, S., Huang, H.J., and Lin, J.F. (2016) Elasticity of single-crystal NAL phase at high pressure: A potential source of the seismic anisotropy in the lower mantle. Journal of Geophysical Research, 121(8), 5696–5707.

Wysession, M.E., Langenhorst, A., Fouch, M.J., Fischer, K.M., Al-Eqabi, G.I., Shore, P.J., and Clarke, T.J. (1999) Lateral variations in compressional/shear velocities at the base of the mantle. Science, 284(5411), 120–125.

Xu, S.Z., Lin, J.F., and Morgan, D. (2017) Iron partitioning between ferropericlase and bridgmanite in the Earth's lower mantle. Journal of Geophysical Research, 122(2), 1074–1087.

Yamazaki, D., and Karato, S. (2001) Some mineral physics constraints on the rheology and geothermal structure of Earth's lower mantle. American Mineralogist, 86, 385–391.

Yamazaki, D., Yoshino, T., Matsuzaki, T., Katsura, T., Yoneda, A. (2009) Texture of (Mg,Fe)SiO$_3$ perovskite and ferro-periclase aggregate: implications for rheology of the lower mantle. Physics of the Earth and Planetary Interiors, 174(1-4), 138–144.

Yang, J., Mao, Z., Lin, J.F., and Prakapenka, V.B. (2014) Single-crystal elasticity of the deep-mantle magnesite at high pressure and temperature. Earth and Planetary Science Letters, 392, 292–299.

Yang, J., Tong, X.Y., Lin, J.F., Okuchi, T., and Tomioka, N. (2015) Elasticity of ferropericlase across the spin crossover in the Earth's lower mantle. Scientific Reports, 5, 17188.

Yang, J., Lin, J.F., Jacobsen, S.D., Seymour, N.M., Tkachev, S.N., and Prakapenka, V.B. (2016) Elasticity of ferropericlase and seismic heterogeneities in the Earth's lower mantle. Journal of Geophysical Research, 121(12), 8488–8500.

Yoneda, A. (1990) Pressure derivatives of elastic constants of single crystal MgO and MgAl$_2$O$_4$. Journal of Physics of the Earth, 38(1), 19–55.

Zerr, A., and Boehler, R. (1994) Constraints on the melting temperature of the lower mantle from high-pressure experiments on MgO and magnesiowüstite. Nature, 371, 506–508.

Zha, C.S., Mao, H.K., and Hemley, R.J. (2000) Elasticity of MgO and a primary pressure scale to 55 GPa. Proceedings of the National Academy of Sciences, 97(25), 13494–13499.

Zhang, J.S., and Bass, J.D. (2016) Sound velocities of olivine at high pressures and temperatures and the composition of Earth's upper mantle. Geophysical Research Letters, 43(18), 9611–9618.

Endnote:

[1]Deposit item AM-19-26656, Supplemental Figures and Tables. Deposit items are free to all readers and found on the MSA website, via the specific issue's Table of Contents (go to http://www.minsocam.com/MSA/AmMin/TOC/2019/Feb2019_data/Feb2019_data.html).